Landmarks in Earth Reinforcement, - Ochiai et al (eds),
© 2003 Swets & Zeitlinger, Lisse, ISBN 90 265 1863 3

Full-scale performance testing and numerical modelling of reinforced soil retaining walls

R.J. Bathurst, D.L. Walters & K. Hatami
GeoEngineering Centre at Queen's-RMC, Geotechnical Group, RMCC, Kingston, Ontario, Canada

T.M. Allen
Washington State DOT, FOSSC Materials Laboratory, Olympia, WA, USA

ABSTRACT: The paper presents the results from an on-going program of full-scale tests of geosynthetic and metallic reinforced soil retaining walls carried out by the Geotechnical Group at the Royal Military College of Canada. The paper describes the test program, some instrumentation details and selected results from six test walls. Five of the walls were constructed with a column of dry-stacked modular concrete units and one nominally identical wall was constructed with a very flexible wrapped-face. All of the structures were surcharge loaded to stress levels well in excess of working load conditions. The data gathered from this program has been useful to identify important performance features and to highlight possible sources of conservatism in current methods of analysis for reinforced soil structures in North America. The high quality data is being used to calibrate numerical models. Examples of numerical simulation results of wall performance at the end of construction and lessons learned are presented and discussed.

1 INTRODUCTION

The Geotechnical Group of the Civil Engineering Department at the Royal Military College of Canada (RMCC) is engaged in an on-going research project related to the design, performance and numerical modelling of reinforced soil structures. A major component of this research has been the construction, surcharge loading and monitoring of carefully instrumented full-scale geosynthetic and metallic reinforced soil retaining walls.

The principal objectives of the experimental work are:

1. Develop a better understanding of the mechanical behaviour of reinforced soil walls during construction, at working load levels and under uniform surcharge loading approaching collapse of the structures.
2. Create a database of results from carefully instrumented full-scale walls that can be used to calibrate numerical models.
3. Use the lessons learned from full-scale tests to improve current design methodologies for reinforced soil retaining walls.

The long-term research program involves the construction of 10 walls. Six walls have been completed and the seventh wall is under surcharge loading at the time of this paper. Each of the walls was 3.6 m in height. Five of the walls were constructed with a column of dry-stacked modular concrete units (NCMA 1997, Bathurst & Simac 1994) and one nominally identical wall was constructed with a very flexible wrapped-face. Following construction, all of the structures were stage uniform surcharge loaded to stress levels well in excess of working load conditions. Figure 1 shows a typical reinforced soil segmental retaining (SRW) wall structure from this test program.

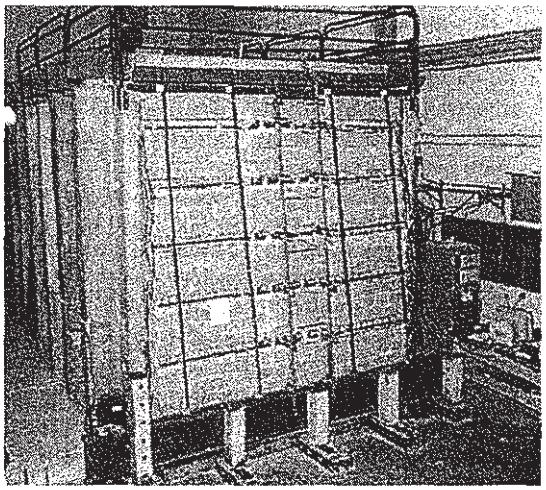

Figure 1. Reinforced soil segmental retaining wall (Wall 1).

The paper first presents an overview of the experimental program, some selected results and implications of wall performance to current design methods in North America. Next, details of numerical modelling of selected walls and comparisons of predicted results using the program FLAC (Itasca 1998) are presented and compared to measured data.

The results of this paper will be of interest to researchers engaged in the development of improved

design methods for both geosynthetic and metallic reinforced soil walls. The data will also be of interest to modellers who require high quality data to calibrate numerical models which can then be used to extend the database of physical test results reported herein to a wider range of wall geometry, facing types, reinforcement and soil materials.

1.1 *RMCC Retaining Wall Test Facility*

The full-scale walls were constructed in the RMCC Retaining Wall Test Facility located within the Civil Engineering Department structures laboratory. This test facility was constructed to provide a general purpose, large-scale apparatus to test a variety of reinforced soil structures (Bathurst 2000, Bathurst et al. 2000). Figure 2 presents a schematic of the test facility. The facility allows soil retaining wall structures to be constructed that are 3.6 m high by 3.4 m wide with the backfill soil extending to a distance of 6 m from the front edge of the facility. The facility offers the advantages of construction and monitoring of soil retaining wall structures in a controlled indoor environment.

The principal structural components of the facility are six heavily reinforced concrete counterfort-cantilever wall modules that are bolted to the laboratory strong floor. Approximately 70 m^3 of backfill soil is placed and laterally contained between the counterfort walls and seated on the rigid concrete foundation. The inside surfaces of the test facility (side walls) are constructed with a composite of plywood, plexiglass and polyethylene sheets to reduce side wall friction. The polyethylene sheets are lubricated using a silicone-based high temperature bearing grease. Results from shear box testing of exhumed specimens of the multi-layer friction reducing layers showed that the peak soil-side wall interface friction angle varies from 15 degrees at a normal pressure of 6 kPa to about 2 degrees at a normal pressure of 60 kPa. Three dimensional stability analyses have shown that the contribution of the test facility side walls to boundary tractions on an internal Coulomb wedge of soil is less than 15 percent of the total active earth force that would be resisted by a stiff facing under true plane strain conditions and incipient collapse of the soil (Bathurst 1993). The magnitude of this difference is within the accuracy of many of the measurements recorded in a typical experiment.

The toe of each full-scale wall is located at the front of the test facility while the back of the soil mass is restrained by a series of rigid reinforced concrete bulkheads. Six rectangular hollow steel sections at the top of the facility are attached to bolts that extend through the counterfort walls to the laboratory strong floor. These sections act as the restraining system for a timber joist and plywood ceiling. The ceiling in turn confines a series of air bags that are used to apply a uniform surcharge to the entire soil surface. The air bags are in-expensive

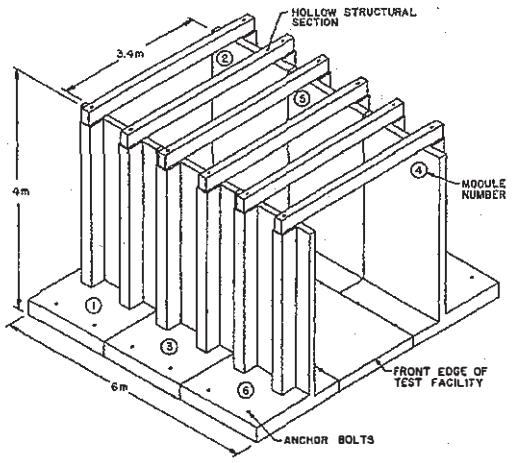

Figure 2. RMCC Retaining Wall Test Facility.

commercially available products made of a paper shell that encapsulates a polyethylene bladder. Air pressure is supplied to the test facility from the central air compressor for the laboratory. An adjustable mechanical regulator is used to attenuate any fluctuation in the air pressure supplied to the air bags. Uniform surcharge pressures up to 130 kPa (equivalent to an additional 7-m height of fill) have been applied to test walls using the surcharging arrangement described here.

1.2 *General*

Table 1 summarises the essential details and objectives of the first six test walls in the research program. The modular facing units for the SRW structures (Walls 1, 2, 3, 5, and 6) were a solid masonry block with a continuous concrete shear key. The blocks are 300 mm long (toe to heel), 150 mm high, 200 mm wide and have a mass of 20 kg. The wall facing units were built with a staggered (running joint) pattern matching the construction technique used in the field (Figure 1). The target setback of each layer of blocks corresponds to a facing batter of 8 degrees from the vertical. The 3.4-m wide modular block facing was constructed in three discrete panels (columns) - two 1.2-m wide outside sections and a central 1-m wide panel. The central column section and its footing support were isolated from the outside sections to further decouple the instrumented central panel section from the influence of the test facility side walls. The reinforcement was also discontinuous at the locations of the two vertical cuts in the wall facing. Only the 1-m wide reinforcement strips over the central 1-m width of the test facility were instrumented.

1.3 *Soil*

Figure 3 shows the particle size distribution curve for the sand backfill used in the tests. The material is a clean uniform size rounded beach sand (SP) with a constant volume friction angle $\phi_{cv} = 35°$ and a peak

Table 1. Full-scale test wall program.

Wall	Description	Objectives/Variables
1	Geosynthetic wall with modular block facing, using a weak biaxial polypropylene (PP) geogrid with 0.6 m spacing (CONTROL)	Reference wall for evaluating the effect of layer spacing, reinforcement stiffness and strength
2	Geosynthetic wall with modular block facing, using the same weak biaxial PP geogrid as Wall 1, but with alternating longitudinal members removed to produce a geogrid with one half stiffness and strength (0.6 m spacing)	Influence of reinforcement stiffness and strength on reinforcement loads/strains/wall deformations and overall level of safety
3	Geosynthetic wall with modular block facing, using a weak biaxial PP geogrid (0.9 m spacing)	Influence of large reinforcement spacing on reinforcement loads/strains/wall deformations and overall level of safety
4	Geosynthetic wall with a very flexible wrapped-face using a weak biaxial PP geogrid (0.6 m spacing)	Influence of facing stiffness and wall toe restraint on reinforcement loads/strains/wall deformations and overall level of safety
5	Geosynthetic wall with modular block facing, using a polyester (PET) geogrid with similar index strength to the control weak biaxial PP geogrid (0.6 m spacing)	Influence of creep deformation/behaviour on reinforcement loads/strains/wall deformations and overall level of safety
6	Generic steel welded wire mesh (WWM) (14 gauge welded wire - 2 mm diameter) reinforced wall using modular block facing (0.6 m spacing)	Influence of reinforcement stiffness on reinforcement loads/strains/wall deformations, as well as factor of safety against reinforcement rupture

plane strain friction angle $\phi_{ps} = 44°$. The sand has a flat compaction curve and was compacted to a dry unit weight of 16.7 kN/m^3 at a moisture content of 3 to 5% using a lightweight vibrating mechanical plate compactor for Walls 1 through 4 and a jumping jack compactor for subsequent structures. However, the first 0.5-m distance directly behind the wall facing was hand tamped to the same density using a rigid steel plate. This precautionary measure was taken to minimise constructed-induced outward deformations of the blocks and reduce compaction-induced lateral stresses against the back of the facing column.

1.4 *Reinforcement*

An extruded biaxial polypropylene (PP) geogrid reinforcement was used in Walls 1 to 4. Wall 5 incorporated a knitted uniaxial PVC-coated polyester (PET) geogrid and Wall 6 was reinforced using a welded wire mesh (WWM) with a wire diameter of 2 mm (14 gauge). Each layer of reinforcement had a total length of 2.52 m measured from the front of the facing column.

Figure 4 shows the in-isolation load-strain response of the reinforcement materials used in the test program. The strength of the PP geogrid at 5% strain was approximately 10 kN/m and the ultimate strength (T_{ult}) about 14 kN/m, based on wide-width testing conducted in accordance with ASTM D4595 specifications. The aperture size for the PP geogrid was 25 mm parallel to the face of the wall (distance between longitudinal members) and 33 mm perpendicular to the face of the wall (transverse members). A second reinforcement product was created by removing every second longitudinal member from samples of the PP geogrid. This modified PP geogrid had a strength that was 50% of the original reinforcement product and an aperture size that was 50 mm parallel to the face of the wall.

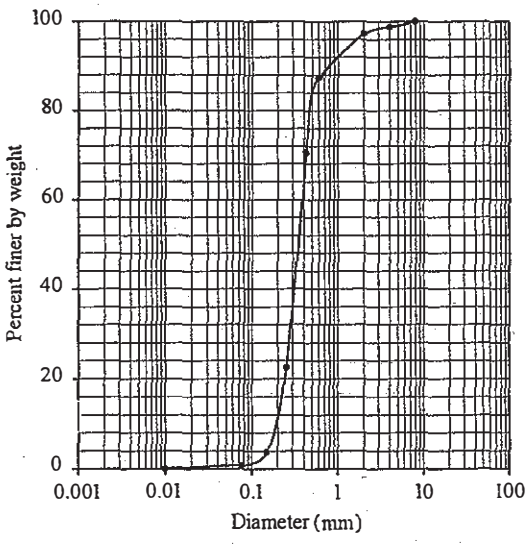

Figure 3. Particle size distribution for the sand backfill soil.

Figure 4 shows that the PET geogrid exhibited a characteristic sigmoidal curve with a strength of 3.5 kN/m at 5% strain and an ultimate strength (T_{ult}) of about 16 kN/m. The PET geogrid was tested in accordance with GRI GG1 specifications for flexible geogrids. The aperture size for the geogrid was 27 mm parallel to the face of the wall (longitudinal

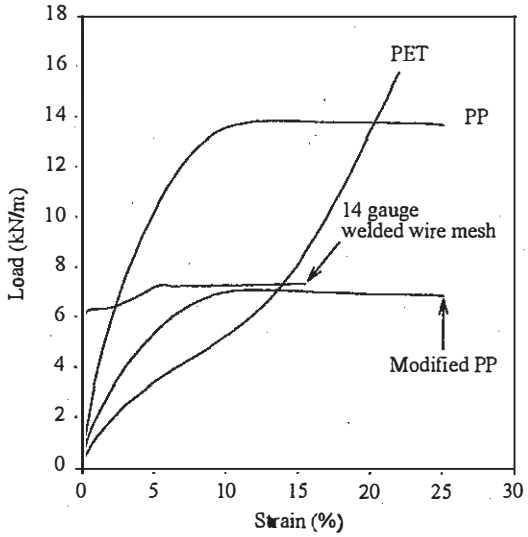

Figure 4. Load-strain response of reinforcement products from in-isolation tensile testing at 10% strain/minute.

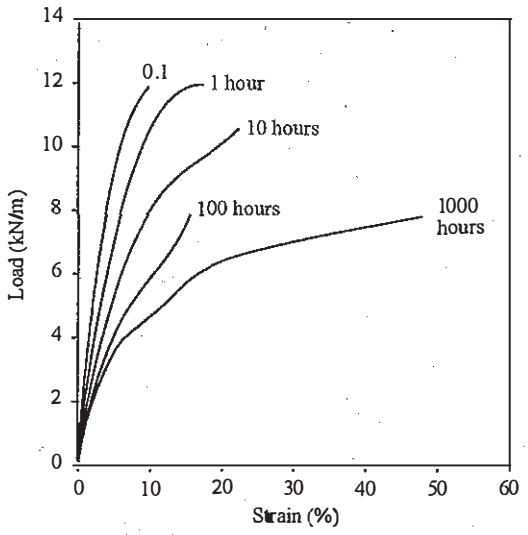

Figure 5. Isochronous load-strain-time curves for the unmodified polypropylene geogrid.

members) and 22 mm perpendicular to the face of the wall (transverse members).

The geogrid reinforcement products used in these full-scale walls are at the very low end of stiffness and strength that is routinely used for geogrid reinforced soil walls in the field. They were specifically selected to generate detectable strains in the reinforcement and to encourage large wall deflections using the available surcharge capacity of the test facility.

The relatively in-extensible WWM employed in Wall 6 was purpose-manufactured with the objective to rupture the reinforcement using the available surcharge capacity of the test facility, generating an ultimate limit state for the structure. The yield strength of the WWM was approximately 6 kN/m, and the ultimate strength (T_{ult}) was about 7.5 kN/m. Strain hardening and ductility was observed for this metallic reinforcement as shown in Figure 4. The aperture size for the mesh was 200 mm parallel to the face of the wall (longitudinal members) and 100 mm perpendicular to the face of the wall (transverse members). The large apertures were required in order to achieve the target ultimate strength of the reinforcement while providing a wire diameter that could be instrumented with strain gauges.

In-isolation constant load (creep) tests were carried out on specimens of each type of geogrid in order to determine the isochronous load-strain properties using the method described by McGown et al. (1984). The creep tests were carried out at 20 ± 1° C, matching the soil temperature in the test walls. Figure 5 shows isochronous load-strain-time curves for the unmodified PP geogrid. The linear portion of each plot is restricted to very low load levels. The plots are highly non-linear which is consistent with the non-linear visco-elastic-plastic behaviour expected from drawn PP geogrid products when subjected to tensile loading.

Figure 6 shows isochronous load-strain-time curves for the PET geogrid. The plots in the figure fall within a narrow band indicating that the PET geogrid stiffness is relatively less affected by time and strain level compared to the PP geogrid. The curves are also non-linear and tend to a sigmoidal shape, which is similar to the trend observed for the index strength test data.

In-isolation isochronous stiffness values of the unmodified PP geogrid and the PET geogrid are presented in Figure 7 (i.e. secant slope of the load-strain curves at different load levels and elapsed time). The 60% of ultimate strength (T_{ult}) curves represent the estimated maximum load level experienced by the geogrid walls in this investigation. The data shows that the stiffness of the PP geogrid at a given load is initially greater than for the PET geogrid but diminishes with time. At sufficiently long times, the stiffness of the PP geogrid can be expected to be less than that of the PET geogrid material in this investigation. However, removing every other longitudinal member of the original PP geogrid material will reduce all of the PP stiffness values in the figure by 50% and the stiffness of the modified PP geogrid can be expected to become less than that of the PET geogrid after relatively short load durations.

The isochronous data was subsequently used to infer tensile loads in the reinforcement directly from recorded strains and elapsed time measurements using the approach reported by Bathurst & Benjamin (1990), Bathurst (1990) and Walters et al. (2001). The estimated loads in the reinforcement using this approach were useful as a cross-check on connection loads measured at the facing.

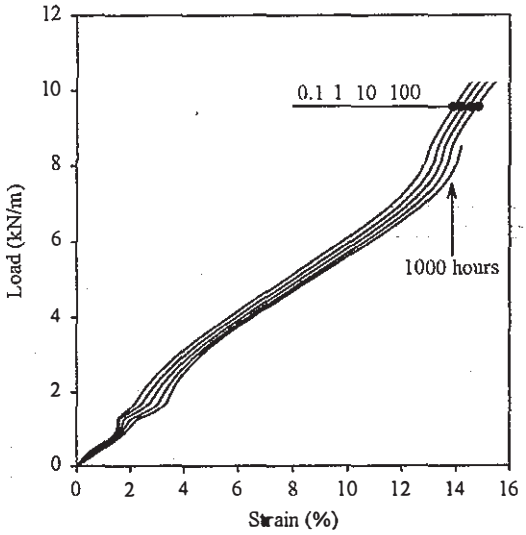

Figure 6. Isochronous load-strain-time curves for the polyester geogrid.

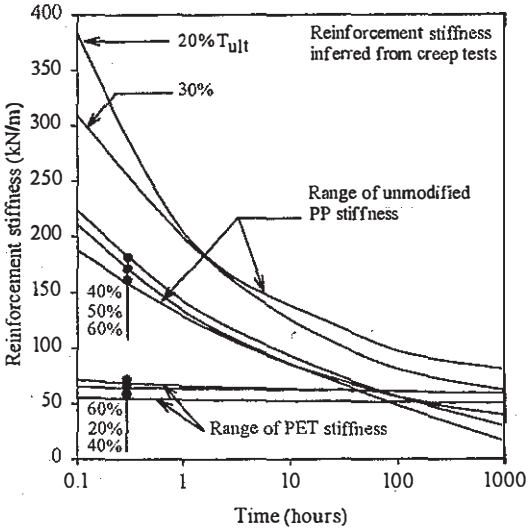

Figure 7. Reinforcement stiffness as a function of load and time.

In-isolation constant rate of strain (CRS) tests were also carried out on geogrid specimens. These results showed that the stiffness of the PP geogrid materials was highly strain-rate dependent while the PET geogrid was less strain-rate dependent. The results of the CRS tests were used to model the reinforcement in numerical simulations presented later in the paper.

1.5 *Instrumentation*

Figure 8 illustrates a typical instrumentation plan for the SRW structures in the test program. A minimum of 300 different electronic devices (instruments) were installed in each test wall in order to record the following measurements:

1. Wall facing deflections.
2. Strain in the reinforcement layers (approximately 100 strain gauges).
3. Connection loads between the facing column and the reinforcement layers (SRW structures).
4. Horizontal and vertical toe loads (SRW structures).
5. Vertical earth pressures at the base of the soil mass and within the soil mass.
6. Vertical deformations within and at the surface of the soil mass.

Connection load rings and load cells at the toe of the wall shown in Figure 8 were not required for the wrapped-face wall (Wall 4). Horizontal displacements of each wall facing were monitored using linear potentiometer-type displacement transducers (potentiometers) located at elevations that corresponded to the reinforcement layers.

The PP geogrid used in the tests has the advantage that it can be easily instrumented using foil strain gauges (rated to 10% strain) bonded directly to the surface of longitudinal members. Bonding the strain gauges to the PET geogrid was accomplished using a special technique developed at RMCC, that included removing the PVC coating and attaching the gauges directly to the polyester bundles. For measurement redundancy, strain gauges were attached at nominally identical distances behind the facing column on different parallel longitudinal members of the reinforcement.

Experience has shown that the local strain recorded by the strain gauges may not be the same value as the average strain recorded over a gauge length that captures many geogrid apertures (Bathurst 1991, Bathurst & Allen 2001). Hence, each combination of gauge type, bonding method and geogrid type must be individually calibrated in order to determine the relationship between local strain and "global" strain using in-isolation index tensile and creep tests. This is particularly important since reinforcement tensile forces inferred from strain readings must be global values for back-analysis purposes (Bathurst 1993, Karpurapu & Bathurst 1995).

The circular cross-section of the WWM longitudinal reinforcement strands was flattened at strain gauge locations. This procedure created a local flat surface that was wide enough to attach the gauges to both sides of the wire. Gauges were attached in pairs to the bottom and top of the wire to cancel out bending strain readings.

Wire-line extensometers were used to measure reinforcement displacements. Each device was comprised of a thin metal cable attached to a reinforcement junction. The line was then passed through a stiff plastic tube (to isolate the cable from the surrounding soil) and attached at the opposite end to a potentiometer that was mounted at the back of the test facility. Displacement readings by selected pairs of extensometer devices were also used to estimate "global" strains in the reinforcement particularly after strain gauges had

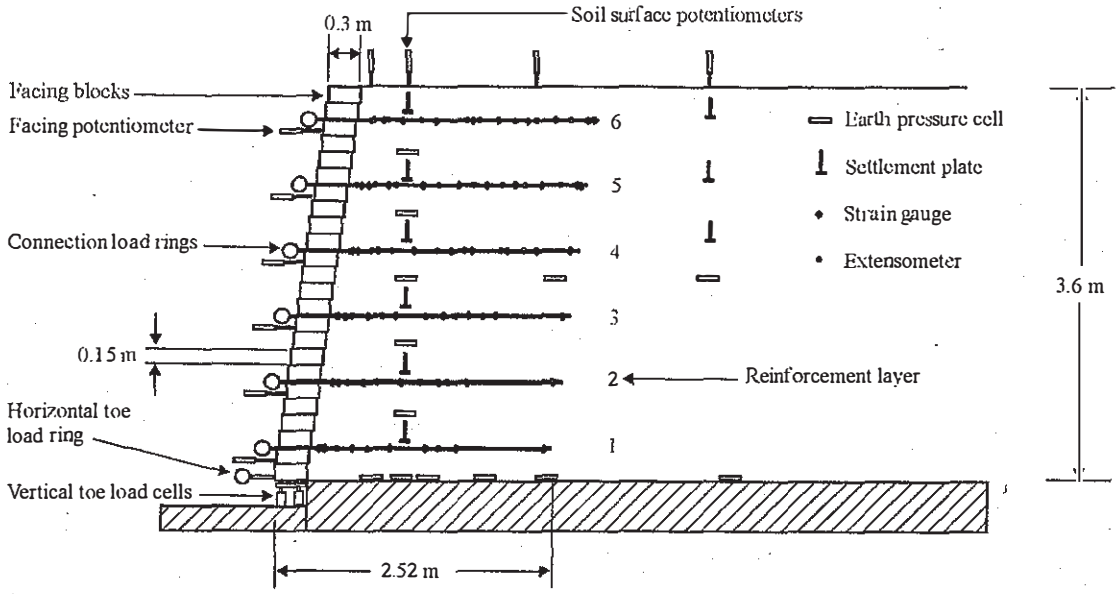

Figu e 8. Typical instrumentation plan for segmental walls.

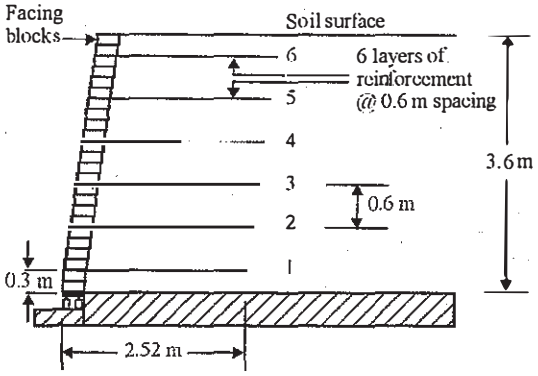

Figure 9. Test configuration for Walls 1, 2, 5 and 6.

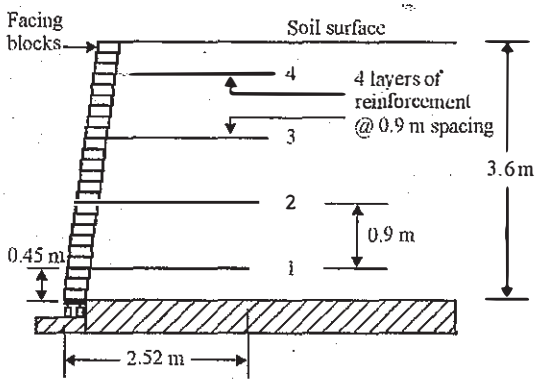

Figure 10. Test configuration for Wall 3.

debonded from the surface of the geogrid after large reinforcement strains.

Selected modular blocks in the facing column for the SRW structures were modified to accommodate load rings that were purpose-built to measure connection loads during construction, surcharging and excavation (Bathurst 1990). To simplify interpretation of test results, the connections were designed so that there was no slip of the reinforcement layers at the interface between the facing block units. Hence, the connection strength was equal to the in-isolation index strength of the reinforcement.

The base of the facing column in the SRW

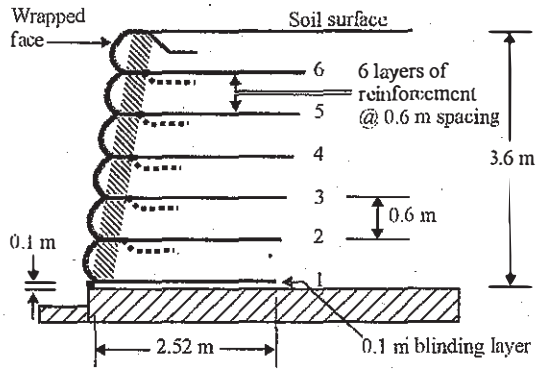

Figure 11. Test configuration for Wall 4.

structures was seated on a rigid steel base plate. The base plate was supported in turn by a roller plate arrangement. Two rows of load cells were located directly below the roller plate to measure the vertical component of the forces at the toe and heel of the facing column. A row of load rings connected to the base plate was used to monitor the horizontal forces and to restrict horizontal movement at the base of the wall to less about 2 mm during construction and surcharging. Hence, the base of the facing column (footing) was fully restrained with respect to the vertical direction but was allowed to deform slightly

in the horizontal direction. The load cells and load rings at the base of each facing column allowed the de-coupled vertical and horizontal footing load components to be measured independently for the duration of each experiment.

Vertical earth pressures at the base of the backfill were measured using earth pressure cells that were securely embedded in a plaster-of-Paris mix on the concrete foundation of the test facility. Earth pressure cells were also placed between reinforcement layers to investigate the influence of the reinforcement inclusions on earth pressure distribution within the backfill.

Potentiometers were used to measure the vertical displacements of settlement plates located on the surface and within the sand backfill. Horizontal deformation of the backfill was inferred from the displacements recorded at the facing column and along the reinforcement layers.

An automated data acquisition system was used to record all instruments at programmed intervals during construction, surcharging and excavation. The data was exported to prepared spreadsheets so that a complete record of wall performance was available within a few hours of data downloading. In this way current data was available to make rapid decisions regarding the surcharge loading program.

1.6 *Test configurations and surcharging*

Test configurations for Walls 1 through 6 described in Table 1 are illustrated in Figures 9 to 11.

Wall 1 (Figure 9) was constructed with six layers of the control PP geogrid at a spacing of 0.6 m. The wall was designed to satisfy current National Concrete Masonry Association guidelines (NCMA 1997). An additional design constraint was that the reinforcement layer spacing not exceed a distance equal to twice the modular block toe to heel dimension (AASHTO 1996). This wall is the control or reference case for the remaining wall structures in the current research program.

Wall 2 (Figure 9) was constructed in an identical manner to Wall 1 except that the modified PP geogrid was used as the reinforcement. Hence the reinforcement in this wall had 50% of the strength and 50% of the stiffness of the reinforcement used in the control structure. This was done to isolate the influence of reduced reinforcement strength and stiffness on wall performance.

Wall 3 (Figure 10) was constructed in an identical manner to Wall 1 except four layers of the PP geogrid were used instead of six layers. This wall allowed the influence of reinforcement spacing to be isolated.

Wall 4 (Figure 11) was constructed with six layers of the PP geogrid but without the hard facing. The reinforcement was arranged to form a very flexible wrapped-face in order to isolate the influence of the facing stiffness on wall performance (i.e. compare performance of Wall 4 to Wall 1). The

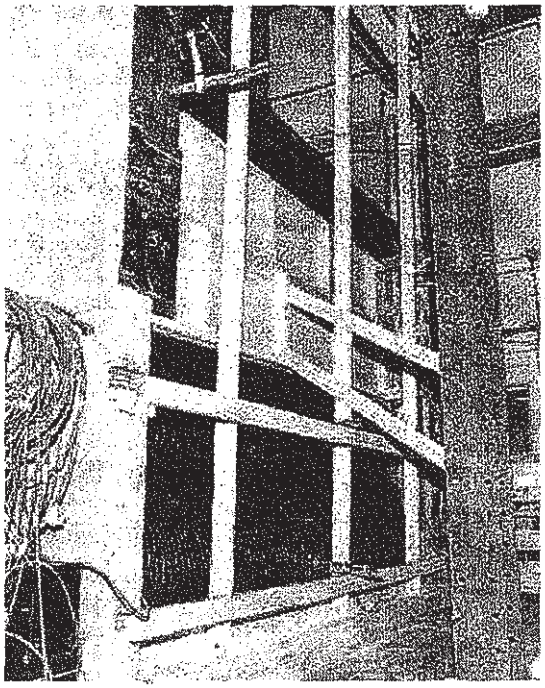

Figure 12. Moving formwork technique for Wall 4.

wall was constructed on a thin (10-mm thick) blinding layer to lift the first reinforcement layer above the concrete foundation. Figure 12 shows the "moving formwork" technique used in the construction of this wall. The forms were braced against the front of the test facility to maintain a target facing batter of 8 degrees from the vertical. Two wrapped-face layers were supported simultaneously during construction. The shaded zone close to the face of the structure in Figure 11 corresponds to the cross-section occupied by the equivalent stacked modular block facing in the SRW structures. Each facing wrap was attached to the reinforcement layer above using a metal bar clamp. With the exception of the top layer, each facing wrap was not extended back into the reinforced soil zone corresponding to the dashed lines in Figure 11. Hence, the geometry and reinforcement attachment used in Wall 4 does not correspond to a typical wrapped-face construction. The construction technique used in this investigation was purposely adopted to facilitate quantitative comparison of walls built with a hard face (stiff) and a nominally identical wall built with an idealised very flexible face.

Wall 5 (Figure 9) was constructed in an identical manner to Wall 1 but with the PET geogrid used for the reinforcement. This wall was designed to isolate the influence of reinforcement visco-elastic-plastic (creep) properties and reinforcement stiffness on wall performance.

Wall 6 (Figure 9) was reinforced with the welded wire mesh (WWM) material to further investigate the influence of reinforcement stiffness on wall performance.

Figure 13 shows the construction rate for the six test walls. Time zero in the plot corresponds to the time when the first layer of sand was placed in the test facility. The construction of Wall 1 proceeded slowly as the research team developed experience with the construction technique. Subsequent walls, with exception of an equipment delay for Wall 6, were constructed more rapidly. Wall 4 (wrapped-face) was constructed in the shortest period of time (about 450 hours) since facing blocks and connection load rings were not present. It may be noted that the construction rate for these test walls is slower than for typical field cases. Construction rate is a factor when attempting to estimate reinforcement loads from in-isolation creep and CRS data (Walters et al. 2001).

Following construction, each wall was subjected to staged uniform loading using the airbag system described earlier. Figure 14 illustrates the

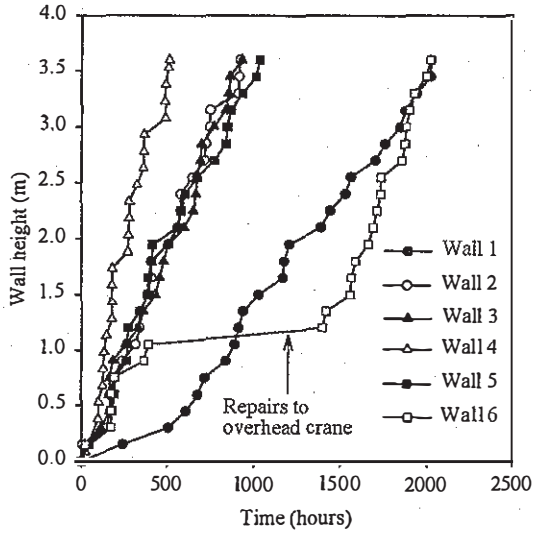

Figure 13. Construction history for RMCC test walls.

surcharging history for Wall 5. Based on the experience gained from Wall 1, the duration of each surcharge load increment was kept constant for about 100 hours, or more, in order to allow time-dependent deformations in the system to come to equilibrium. At the end of the surcharging program (return to zero surcharge load) the toe was released for each SRW structure to examine the influence of the horizontally restrained toe on wall performance.

Finally, each wall was carefully excavated in 300-mm deep layers while monitoring strain gauges and extensometers attached to each reinforcement layer. In this way, the location of internal failure surfaces through the reinforced soil mass could be visually confirmed and strain recovery in the reinforcement layers due to removal of the overburden recorded.

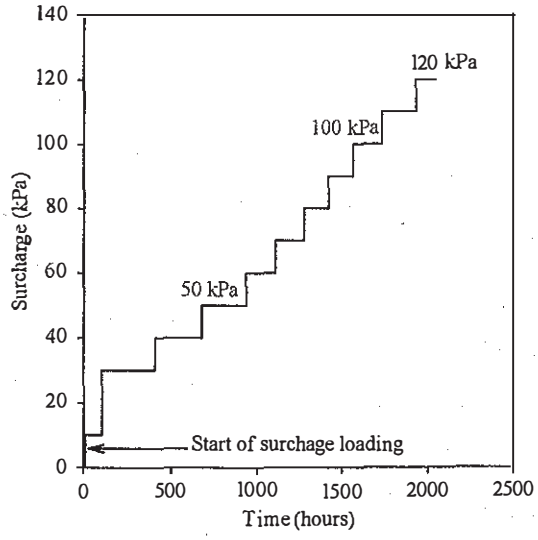

Figure 14. Surcharge history for Wall 5.

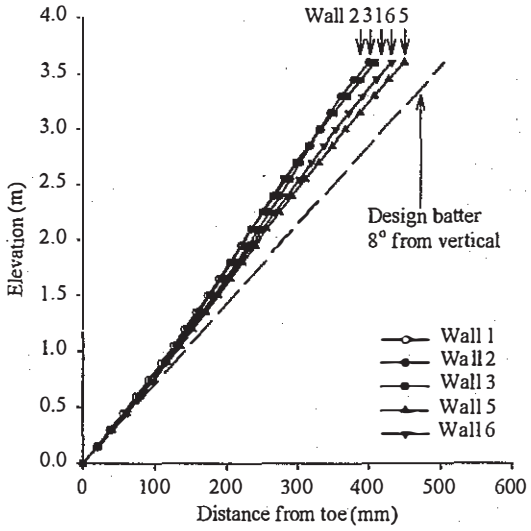

Figure 15. Facing column profiles at end-of-construction for segmental walls.

2 PERFORMANCE

2.1 *Facing column profiles*

Figure 15 shows the results of potentiometer readings used to calculate the facing column profiles for the SRW structures at the end of construction. The dashed line in the figure is the target facing batter based on the geometry of the block units and the built-in concrete shear key location. This is the profile of the wall face if the blocks could be placed without backfill and each unit pushed forward against the shear key on the underlying blocks. The figure shows that the actual facing alignment for the control structure (Wall 1 - 6 layers of PP) is steeper than the target batter as a result of the incremental

construction of the facing column together with fill placement and compaction. The data in the figure also shows that significant differences in the end-of-construction profiles for the three PP geogrid walls were not detectable for the range of stiffness values and vertical spacing used.

The interpretation of the relative performance of Walls 6 (WWM) with respect to the PET geogrid wall (Wall 5) is more difficult. The larger outward deformations of the welded wire mesh wall compared to the PET wall may be counter intuitive since the stiffness of the WWM material is approximately 50 times that of the PET wall material (and 10 times that of the control PP material used in Wall 1). However, the welded wire mesh had an aperture size of 200 x 100 mm compared to 27 x 22 mm for the PET material. Hence, the load transfer between the wire mesh and the sand backfill at low confining pressures may be less than that for the PET material.

The PET geogrid used in Wall 5 had the smallest opening sizes of all the reinforcement products used (27 x 22 mm) and the roughest surface. Therefore the relatively stiff response of the facing column during construction may be due to greater interface stiffness and interlock with the sand under low confining pressures. Nevertheless, the assignment of different mechanical properties of the reinforcement materials and number of reinforcement layers to account for differences in magnitude of construction-induced movement of otherwise identical walls must be undertaken with caution. The magnitude of outward deformations is sensitive to construction technique including small variations in compaction effort behind the facing column. From a practical point of view it may be argued that despite the range of reinforcement aperture size, surface roughness, reinforcement spacing, reinforcement stiffness and global wall stiffness, the maximum construction-induced wall movement varied over a narrow range of 1 to 3%. This observation supports the argument that construction teclmique for a given facing type is an important factor controlling construction-induced wall deformations in the field. The influence of reinforcement stiffness on wall deformations can be detected more easily from measurements made during the post-construction surcharging of the walls (see Section 2.7).

Figure 16 compares the surveyed facing profile of Wall 1 (control hard-faced wall) and Wall 4 (wrapped-face) at the end of construction. Not unexpectedly, the very flexible wrapped-face wall can be seen to have displaced by about 250 mm at the base of the wall. This movement was generated largely at the time the bottom formwork was removed after construction of the two lowermost layers of reinforcement. Nevertheless, the target batter of 8 degrees was reasonably well achieved for the remaining reinforcement layers.

Figure 17 presents the history of wall deflections recorded for Wall 1. The horizontal deflections were recorded at reinforcement elevations on the outside of the facing column and are taken with respect to the time of installation of the measurement device during wall construction. Each jump in a deflection

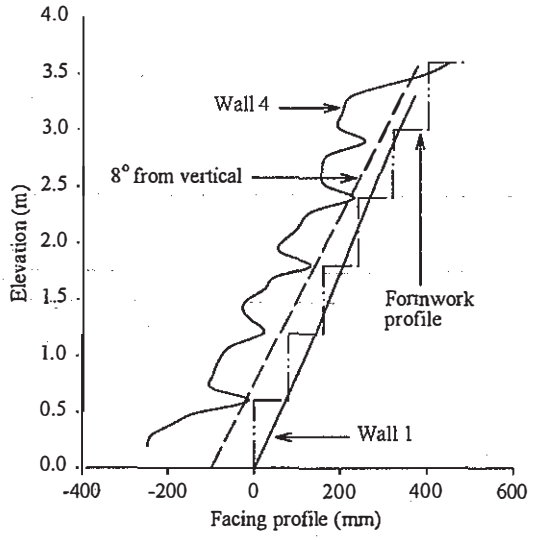

Figure 16. Facing column profiles at end-of-construction for segmental Wall 1 and wrapped-face Wall 4.

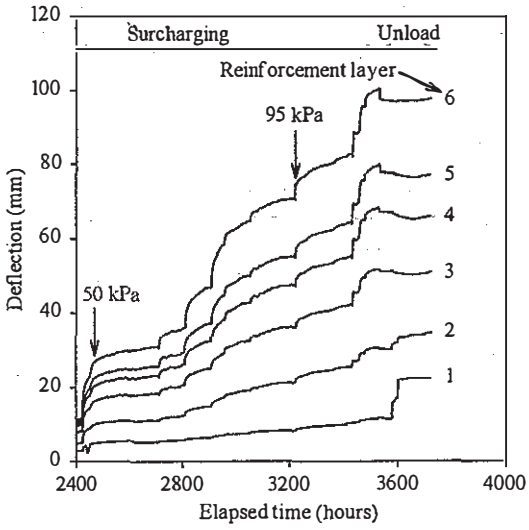

Figure 17. Horizontal deflections measured at face of Wall 1 opposite reinforcement layers.

curve corresponds to the application of a new surcharge load. Time-dependent displacements of the structure under constant load (creep) are clearly evident in the figure. For Wall 1, the greatest deflections were recorded close to the crest of the wall, which is a direct consequence of the heavy surcharge loads applied to the backfill soil and the restrained toe boundary at the base of the structure.

Figure 18 shows facing profiles for Wall 2 taken with respect to the end-of-construction profile. Post-construction bulging of the facing column during surcharge loading is evident in the figure and the apex of the bulge occurs at an elevation of about 3/4 of the height of the wall. The greatest change in the facing profile for Wall 2 occurred during the application of the 50-kPa load level. The large incremental change in wall deflection may be the

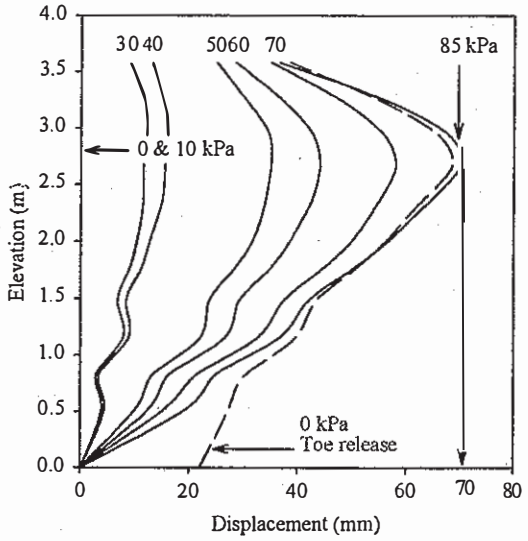

Figure 18. Facing profiles for Wall 2 taken with respect to end-of-construction.

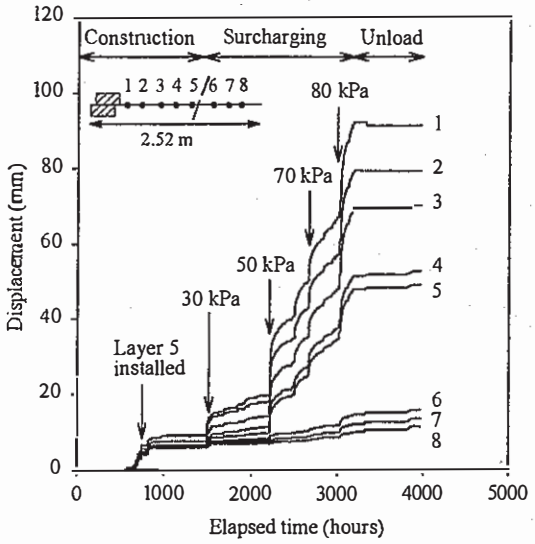

Figure 19. Extensometer displacements recorded for reinforcement layer 4 of Wall 2.

result of load shedding from the soil to the reinforcement layers consistent with development of an internal failure of a wedge of reinforced soil. At the end of surcharging the maximum post-construction displacement was approximately 70 mm corresponding to about 2% of the height of the wall.

At the end of the test, the surcharge load was removed, the horizontal toe restraint released and the base of the wall allowed to move outward by about 20 mm. Outward movements of the base of the facing column after the toe was released were observed in all of the hard-faced walls in this test program. Clearly, soil pressures acting on the back of the stiff facing column were transmitted to the horizontally restrained footing.

2.2 *Reinforcement displacements and strains*

Figure 19 illustrates the history of reinforcement displacements recorded by extensometers attached to layer 4 of Wall 2. The entire group of extensometers moved simultaneously by about 5 mm between the time of installation of the reinforcement layer and the installation of layer 5 located 0.6 m above. After further backfill placement and the application of the surcharge loads, interlock between the backfill and the reinforcement was mobilised and load transfer between the reinforcement and soil occurred.

The time-dependent deformation of the reinforcement layer during surcharge loading is evident in the data. Upon the application of each surcharge load increment there was a corresponding jump in the extensometer movement followed by time-dependent deformations that increased in magnitude but at a decreasing rate until the application of the next load increment. As expected, the horizontal displacements in each reinforcement layer were largely irrecoverable after surcharge unloading. The plots in the figure also show that relatively small magnitudes of movement were recorded by the three extensometers located closest to the free end of the reinforcement layer (points 6, 7 and 8). This behaviour is consistent with the conventional notion that distinct active and anchorage soil zones develop at incipient collapse of a reinforced soil mass.

In many cases the recorded displacements of the extensometers closest to the facing column were greater than the purely horizontal movement recorded by potentiometers mounted opposite the reinforcement layer on the wall face (compare post-construction displacement of extensometer 1 of Figure 19 to displacement profiles at 85 kPa surcharge pressure in Figure 18). The explanation for this apparent discrepancy is that displacements recorded by an extensometer represent the total in-plane movement of the instrumented reinforcement point and therefore this reading also captures changes in extensometer length due to downward movement of the reinforced soil mass directly behind the facing column.

Figure 20 shows the distribution of strains in selected reinforcement layers at the end of construction of Wall 2. The plot shows that the strains are low (less than 1%) but that they are, nevertheless, largest at the connections and tend to dissipate rapidly along the length of the reinforcement. The figure also shows that the peak strain occurred in reinforcement layer 3, which was at an elevation corresponding to about 1/2 the total height of the wall.

Figure 21 shows the distribution of strains in layer 5 of Wall 2 at different surcharge load levels. Only after the surcharge load reached 50 kPa did a local peak reinforcement strain develop at a location on the reinforcement corresponding to the internal failure plane in the reinforced soil zone. A relatively large jump in the magnitude of strains in this layer can be seen during the application of surcharge load from 40 to 50 kPa which is consistent with the comments made earlier regarding the change in the facing profile illustrated in Figure 18. The multiple

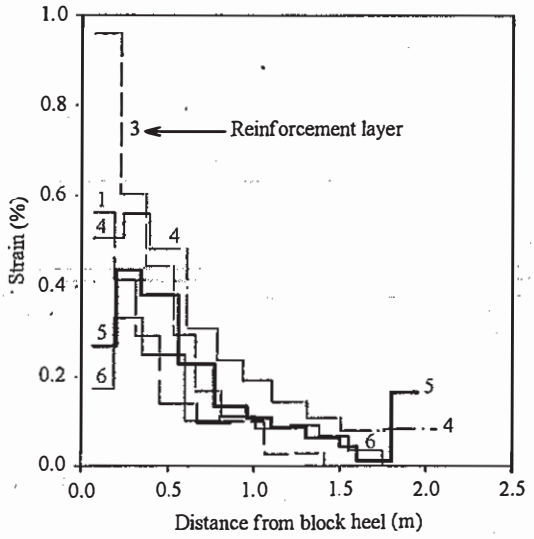

Figure 20. Distribution of strains at the end of construction for Wall 2.

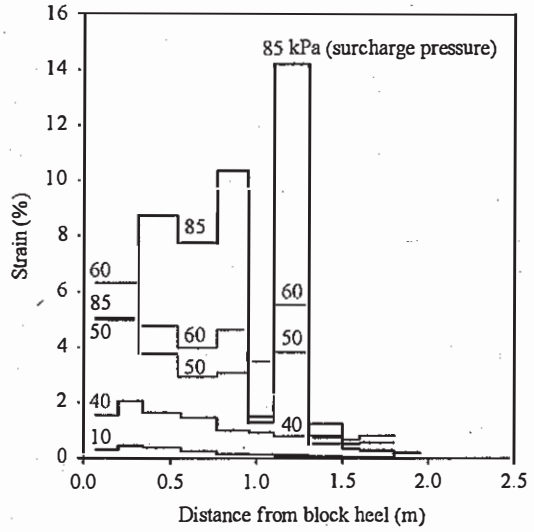

Figure 21. Strain in layer 5 for Wall 2 during surcharge loading.

peaks in the distribution of reinforcement strain observed in Figure 21 during the 85 kPa surcharge load increment may be due to retrogressive failure of the soil in the active zone (i.e. a family of failure surfaces propagating down and back into the reinforced soil zone with increasing surcharge load).

Figure 22 presents the measured strain in the reinforcement at approximately the same elevation (layer 3) for Walls 1 to 5 at the end of construction. The largest measured strains occurred close to the facing in all walls. The strains for Wall 4 (flexible wrapped-face) were as great as six times the magnitude of the strains recorded for the comparable modular block structure (Wall 1) suggesting that the hard facing (stiff) in combination with the restrained footing carries a significant portion of the lateral earth loads.

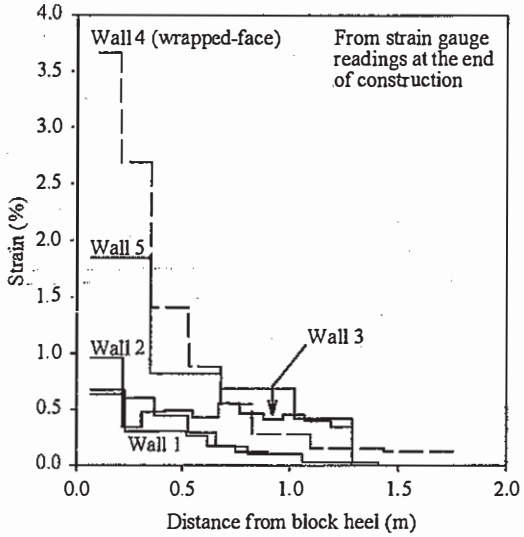

Figure 22. Measured strain at the end of construction in reinforcement layer 3 for Walls 1 to 5.

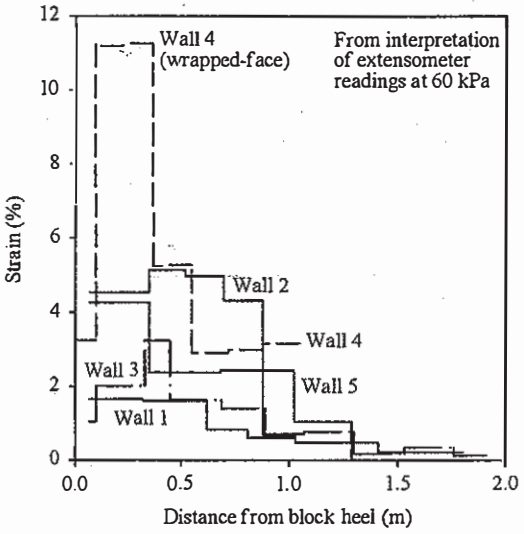

Figure 23. Measured strain at 60 kPa surcharge load in reinforcement layer 3 for Walls 1 to 5.

The relatively high strains at the connections with the hard-faced walls can be attributed to the relative downward movement of the soil behind the facing. This movement occurs as a result of outward rotational movement of the facing column during construction (see Figure 15) and settlement of the sand as a result of compaction during incremental construction. The high strains recorded at the same location in the wrapped-face wall are due to the downward sagging of the wrapped-face (see Figure 16). A similar pattern of peak strains close to the face has been reported by Bathurst et al. (1988) for a wrapped-face wall at end-of-construction. This earlier wall was constructed using a similar reinforcement material but with 750-mm reinforcement spacing and no artificial clamping of the reinforcement layers as described earlier.

At the end of construction, the strains for Wall 3 (four layers of PP geogrid) were generally larger than for Wall 1 (6 layers of PP geogrid) and were observed to propagate deeper into the reinforced soil zone. Similarly, the peak strains for Wall 2 (less stiff PP geogrid) were larger than the strains recorded for Wall 1 constructed with reinforcement having twice the index stiffness. The measured strains in Wall 5 (PET geogrid) at the wall facing were about 2.5 times greater than those recorded for Wall 1 and Wall 3, and about twice those of Wall 2 (all reinforced with PP geogrid). Based on the (short term) in-isolation index test results presented in Figure 4, the PET geogrid would be expected be more extensible than the PP and modified PP geogrids. From Figure 7 the relative performance of these three walls at the end of construction can be explained by the PET isochronous stiffness values that fall below the PP stiffness curves at low load levels.

Figure 23 shows that the magnitude of strains is larger for each wall during the 60-kPa surcharge load compared to the end-of-construction strains in Figure 22. As expected strains are larger under surcharge loading than at end of construction. In Walls 1, 2 and 3 large strain values are observed at locations beyond the connections within the reinforced soil zone. In Figure 23 it can be seen that a 50% reduction in the index reinforcement stiffness resulted in a more than doubling of the measured strain (Wall 2 compared with Wall 1).

The strains measured in Wall 5 (PET) were greater than those for Wall 1 (unmodified PP) which is consistent with the relative stiffness of the two geogrid materials (see Figure 7 where the unmodified PP stiffness curves are above the PET curves at low tensile load levels even after 1000 hours). However, Wall 5 (PET) showed lower strains than Wall 2 (modified PP). Again this can be explained by reference to Figure 7. Removing every other longitudinal member of the original PP geogrid material will reduce all of the PP stiffness values in the figure by 50%. Hence, the isochronous stiffness of the modified PP geogrid can be expected to fall below PET stiffness values even at relatively shorter elapsed times. An additional contribution to larger stiffness of the PET geogrid may be a higher confined modulus than values inferred from in-isolation tests due to compression of the fibres in the longitudinal members, although this is likely to make less than a 10% difference in the stiffness. Finally, the smaller aperture size (27 x 22 mm) of the PET material compared to the modified PP geogrid (55 x 33 mm) may have contributed to greater confined stiffness values. For example, the greater number of transverse members for the PET reinforcement may act to stiffen the longitudinal members.

The coincidence of the location of peak reinforcement strain in reinforcement layers for Wall 2 at peak surcharge load and the internal soil failure surface exposed at excavation is illustrated in Figure 24. The triangle-shaped markers in the figure denote the locations of directly measured peak changes in aperture length measured after reinforcement exhumation. These measurements corroborate the locations of peak strain recorded by strain gauges and inferred from extensometer readings. The failure plane was observed to fit a log-spiral geometry using the peak plane strain friction angle ϕ_{ps} = 44°. However, from a practical point of view the predicted (and simpler) Coulomb failure plane using the same friction angle is reasonably accurate for this height of wall. The triangular markers also indicate the occurrence of retrogressive failure in the active zone. A similar observation was made for the other walls with the exception of Wall 6 (WWM). Although not shown here, the post-construction facing displacements for Wall 6 were not large enough to initiate an internal failure wedge within the backfill.

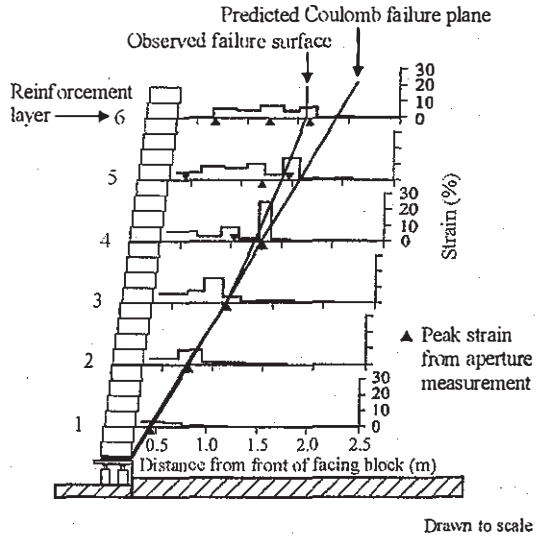

Figure 24. Location of peak reinforcement strain and internal failure surface for Wall2.

2.3 *Connection loads*

Figure 25 shows measured connection loads at the end of construction for each of the hard-faced wall structures. The horizontal toe loads are also plotted on the figure to highlight the contribution of toe restraint to stiff facing column reactions.

For the two PP reinforcement cases investigated with 6 layers of reinforcement (Walls 1 and 2), there appears to be a negligible effect of reinforcement stiffness on magnitude of measured connection loads in 5 of 6 layers. It should be noted that the stiffness of these two products is very low and hence differences in connection loads may be difficult to detect. At layer 2 of Wall 2, local over-compaction and/or a minor difference in seating of the facing units may have contributed to greater connection load at this location.

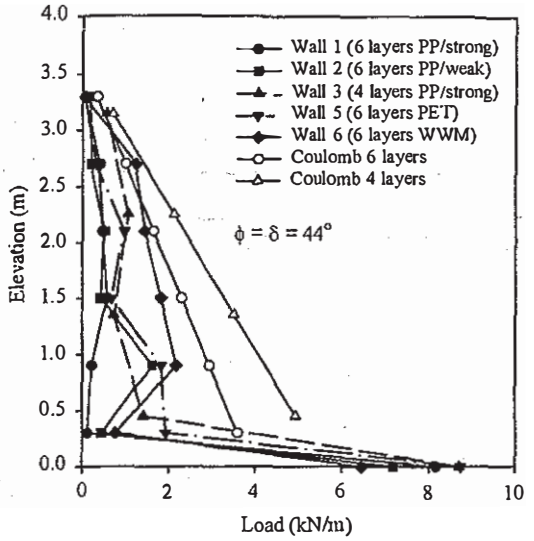

Figure 25. Measured versus predicted connection loads at the end of construction for ϕ = 44 degrees.

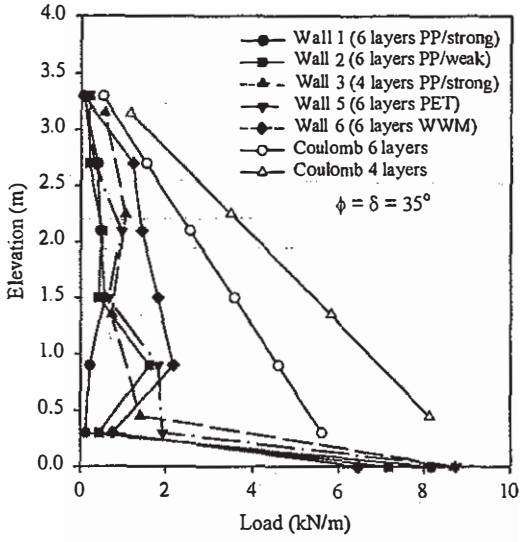

Figure 26. Measured versus predicted connection loads at the end of construction for ϕ = 35 degrees.

The larger reinforcement spacing used in Wall 3 resulted in a larger contributory facing area and hence larger reinforcement loads compared to Wall 1.

Wall 5 (PET reinforcement) recorded larger connection loads than Walls 1 and 2 (PP reinforcement) and a more triangular distribution of the connection loads. The relatively large connection loads observed in the two lowermost layers may have been the result of a change in compaction equipment as described in Section 1.3.

In general, the largest connection loads were observed for Wall 6 that was constructed with a relatively stiff welded wire mesh. The distribution of load for this structure is more triangular with the exception of the bottom-most layer that was in close proximity to the restrained toe of the wall.

Also plotted on Figure 25 are predicted connection loads at the end of construction using Coulomb lateral earth pressure theory calculated using the contributory area approach, peak plane strain friction angle of the soil and, the assumption of fully-mobilised soil-wall friction angle (i.e. ϕ_{ps} = δ = 44°) (NCMA 1997). In contrast to the triangular distribution plotted, the measured connection loads are generally smaller than the Coulomb predictions for all of the walls with polymeric reinforcement and more uniform with depth. The Coulomb-predicted load distribution was most applicable to the wall reinforced with the relatively stiff WWM, except for the deviation from the triangular trend in reinforcement layer 1, which is a direct result of the boundary conditions at the toe of the wall.

Figure 26 compares measured to predicted reinforcement loads based on the constant volume friction angle, ϕ_{cv}, of the soil (i.e. minimum possible friction angle for the soil). The selection of ϕ_{cv} results in an excessively conservative estimate of the reinforcement loads.

The magnitude and distribution of measured connection loads in all of the hard-faced walls is the combined result of the very stiff toe attracting a significant portion of the lateral earth forces, the stiffness of the reinforcement layers, compaction stresses, down-drag forces and, possible redistribution of reinforcement load during construction-induced outward movement of the facing column. Local deviations from trends in connection loads may be attributed to variations in local compaction effort and seating of the modular block facing units.

Taken together, the data in Figures 25 and 26 illustrate that one shortcoming of conventional earth pressure theories applied to reinforced walls with a structural facing is their inability to account for the load that is carried by the restrained toe at the base of a stiff facing column. The discrepancy between measured and predicted values of reinforcement loads is increased by using a constant volume friction angle in Coulomb earth pressure calculations rather than the peak plane strain friction angle.

2.4 *Horizontal and vertical toe loads*

Figure 27 shows the history of vertical toe load forces recorded during construction of Wall 5. Each facing block was individually weighed and hence the self-weight of the facing column during construction can be plotted as the linear line in the figure. Superimposed on the figure is the net vertical footing load and individual loads recorded by two parallel rows of load cells located at the toe and heel of the base plate directly below the facing column (see Figure 8). The sum of the vertical loads is greater than the self-weight of the facing column. This observation is attributed to the vertical down-drag force developed at the connections due to relative downward movement of the sand backfill directly behind the facing column. This downward movement is a result of compaction of the soil and settlement of the soil during outward rotation of the facing column.

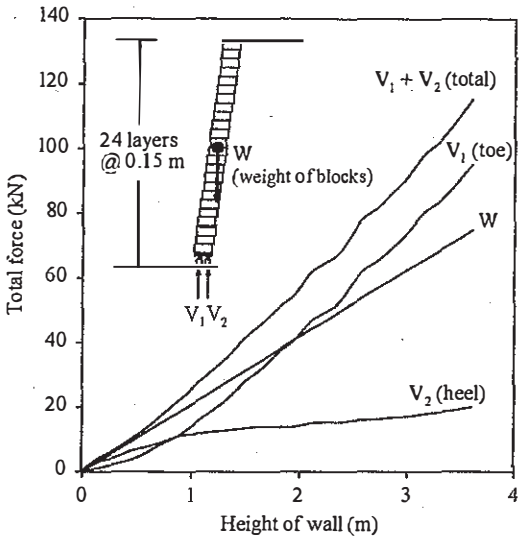

Figure 27. Vertical toe load forces for Wall 5 during construction.

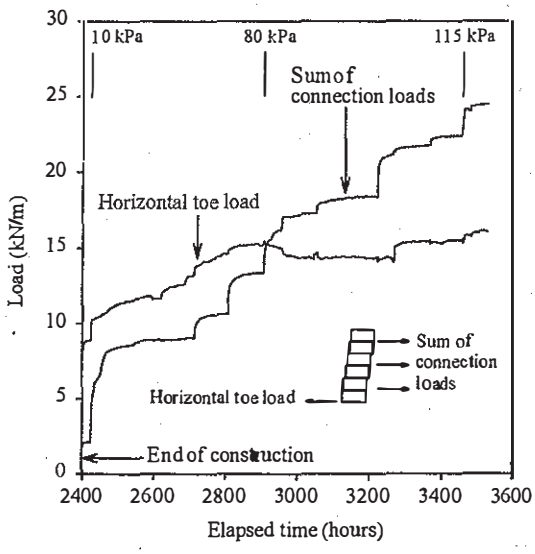

Figure 28. Horizontal toe load at the base of Wall 1 during surcharge compared with the sum of the connection loads.

As the wall was built higher there was a shift of vertical load to the toe of the wall consistent with the notion of wall rotation about the toe of the facing column. However, the heel of each block unit was not unloaded indicating that the batter of the wall was sufficient to keep each block-to-block interface in compression. The hinge height (NCMA 1997, Bathurst et al. 1993) for this structure based on a target batter of 8 degrees is 2.1 m. An important implication of these measurements to the design of the modular block structures in the current study is that the hinge height calculation is conservative for design. Similar observations regarding vertical toe loads were made for the other SRW structures in the test program.

Figure 28 presents the history of horizontal toe load measurements recorded at the base of Wall 1 and the sum of connection loads recorded at the reinforcement layers. The figure shows that the very stiff toe attracted a significant portion of the total horizontal earth force acting against the facing column at the end of construction (approximately 85%). This is not surprising since the toe of the wall is very much stiffer than the reinforcement layers at the end of construction. Furthermore, the stiffness of the facing column helps to transmit lateral earth pressures to the toe. During surcharging, tensile load was mobilised in the reinforcement layers and proportionately more of the horizontal earth force exerted against the facing column was carried by the reinforcement layers. At 80 kPa surcharge pressure, the sum total of the load carried by the reinforcement layers became greater than the horizontal component of the load acting at the toe. Thereafter, the reinforcement layers attracted a greater proportion of the lateral forces generated during each increase in the surcharge load. Nevertheless, the toe carried approximately 40% of the total horizontal earth force recorded at the facing column at the end of the surcharge loading program. The relative contribution of the restrained toe to resist lateral earth pressures can be expected to be a function of wall height. It is reasonable to expect that as the height of a hard-faced (stiff) wall structure increases, the percentage of the total lateral earth forces transmitted to the restrained toe will diminish.

2.5 *Vertical earth pressure*

Figure 29 shows the vertical footing pressure and the distribution of vertical earth pressures recorded by earth pressure cells located at the rigid base of the reinforced soil mass for Walls 1 and 3 at the end of construction. The data indicate that the measured vertical footing pressure is consistently greater than the pressure due to the self-weight of the facing column. This may be attributed to the down-drag forces acting at the back of the facing units due to the reinforcement inclusions (i.e. the column of soil directly behind the facing column can be understood to hang-up on the reinforcement layers at the connections). The data also suggests that an increase in the number of reinforcement layers will increase the magnitude of the down-drag forces (compare Wall 3 with 4 layers of reinforcement to Wall 1 with 6 layers of reinforcement).

The earth pressure measured directly behind the facing column was observed to be less than the calculated pressure due to the self-weight of the sand backfill, with the measured values for Wall 1 less than that for Wall 3. The calculated pressure is based on a vertical wall and hence there will be a reduction in the soil pressure due to the wall batter. However both walls were built with the same facing batter and thus this observation is consistent with the development of vertical load transfer from the soil to the facing column (the greater the down-drag forces, the lower the earth pressure immediately behind the facing column). The plot also shows that the measured earth pressures were greater than the calculated pressure within the reinforced soil zone

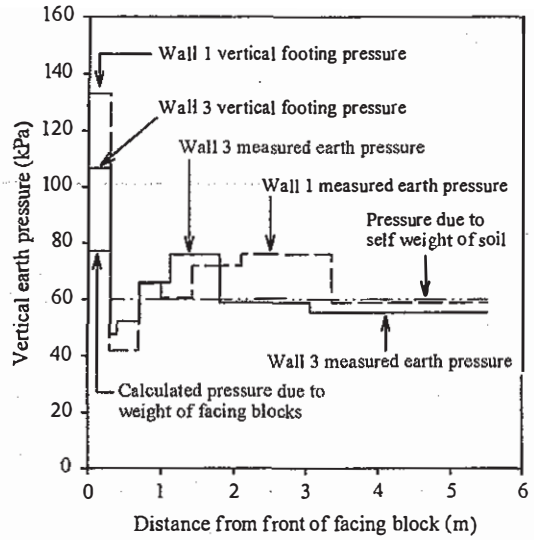

Figure 29. Vertical earth pressure distribution at the base of the backfill soil for Walls 1 and 3 at the end of construction.

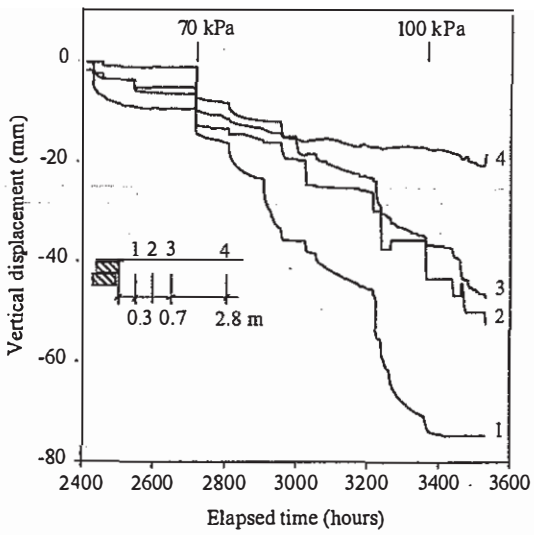

Figure 30. Vertical soil surface deformation for Wall 1 during surcharge loading.

approximately 1 to 3 metres from the face of the wall. This redistribution of the load can be argued to result from vertical equilibrium (i.e. the integrated vertical pressure across the bottom of the structure must sum to zero) and moment equilibrium.

2.6 *Soil settlement*

Figure 30 illustrates the history of the vertical settlement of the backfill during the surcharge loading of Wall 1. The plot shows that there was a noticeable increase in the settlement of the backfill corresponding to the application of a new surcharge load. The largest displacements occurring following the application of the 70-kPa load level. Creep of the SRW structure may be inferred from the plot and the greatest deformations were recorded close to the crest of the wall.

2.7 *Overall wall performance*

Figure 31 shows the overall performance of the reinforced soil SRW structures based on maximum post-construction facing displacements recorded during surcharge loading. In general, for surcharge loads less than 40 kPa, peak wall deflections increased linearly with applied load. Deflections recorded for Wall 5 (6 layers of PET) were greater than those for Wall 1 (6 layers of PP) and about equal to that of Wall 2 (6 layers of PP/weak), which is consistent with the relative stiffness values of the three polymeric reinforcement products at low tensile load levels (Figure 7). The displacements of Wall 1 and Wall 3 (4 layers of PP) were almost identical up to the 40-kPa load level. This would indicate that for these structures, changes in reinforcement spacing had only a minimal influence on overall wall performance. Wall 6 (6 layers of WWM) generated the least facing movement which is consistent with the stiffer load-strain properties of the metallic reinforcement product.

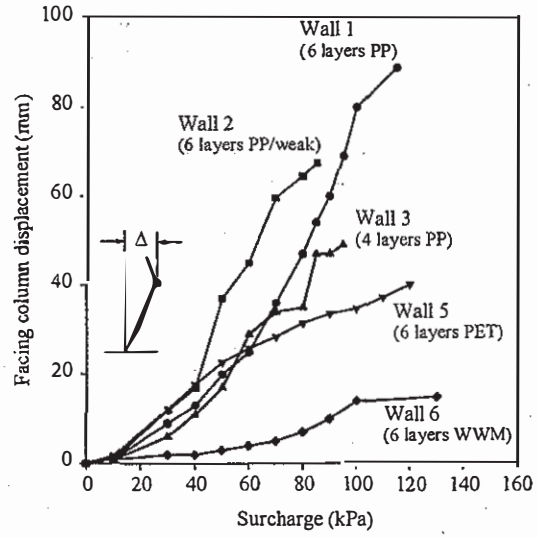

Figure 31. Overall performance of segmental walls based on post-construction facing displacement during surcharge loading.

The figure also shows a highly non-linear response of the walls reinforced with the PP geogrid materials beyond the 40 kPa load level. Facing deflections for Wall 2 were greater than those recorded for Wall 3, which in turn were greater than those for Wall 1 at a surcharge load level of 60 kPa. Beyond the 60 kPa surcharge load level the load increments for Wall 3 were reduced to duration times as low as 0.5 hours (compared to typically 100 hours for the other walls) and hence Wall 3 appears to be stiffer than Wall 1. It is the opinion of the writer's that had the load duration for surcharge levels greater than 60 kPa been maintained at about 100 hours then the displacement-surcharge curve in the figure for Wall 3 would likely have fallen between Walls 1 and 2. This trend would be consistent with the relative global reinforcement

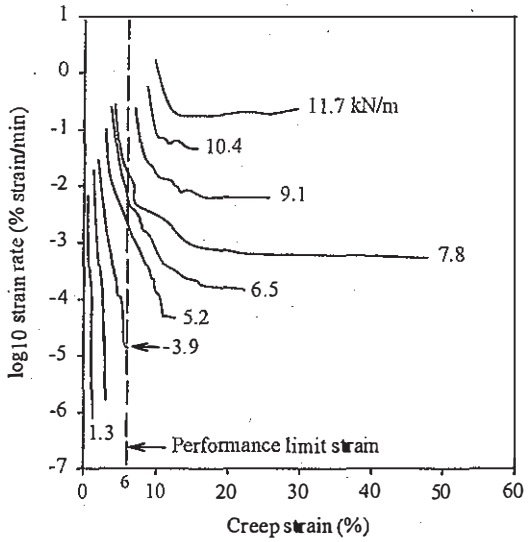

Figure 32. Sherby-Dorn plot for the unmodified PP geogrid.

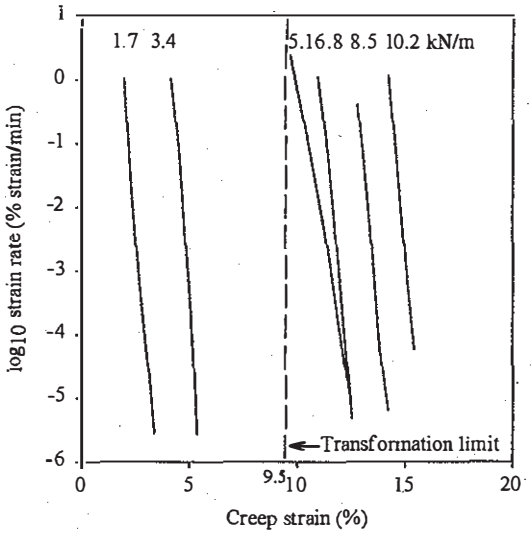

Figure 33. Sherby-Dorn plot for the PET geogrid.

stiffness (S_g) of the walls (i.e. $S_g = \Sigma J/H$ where J is reinforcement stiffness and H is the height of the wall (Allen and Bathurst 2001).

The non-linear response of Walls 1 and 2 reinforced with the PP geogrid to the surcharge loads is consistent with the expected behaviour inferred from the isochronous stiffness curves in Figure 7 (i.e. sharp reduction in stiffness from 30% to 40% of ultimate strength curves).

Figure 32 shows the load-strain properties of the PP geogrid in the form of a Sherby-Dorn plot. Once the performance limit of the material is exceeded, significant increases in the strain and strain rate are possible (McGown et al. 1984). The data in Figure 31 would therefore suggest that the performance limit for the PP reinforced walls was exceeded when the surcharge load was in the range of 40 to 60 kPa.

In contrast, a linear post-construction response was observed for Walls 5 and 6. This indicates that the response of both the PET and WWM reinforced soil systems was essentially elastic in nature.

Figure 33 shows the Sherby-Dorn plot for the PET geogrid which illustrates that the load-strain-time properties of the PET geogrid will be dominated by an elastic response upon the application of the load, with negligible time-dependent strains occurring thereafter. This observation was confirmed when the reinforcement layers were exposed during wall excavation. Measurement of the PET reinforcement aperture sizes indicated that there were no detectable permanent deformations. The transformation limit shown in the figure indicates the approximate load that would initiate the gauche-trans transition that produces the characteristic sigmoidal shape of the PET load-strain curve shown in Figure 4 (Greenwood et al. 2000). The corresponding strain limit (9.5%) was only observed in the top PET reinforcement layer at a surcharge load in excess of 100 kPa.

At the 100 kPa surcharge load level (Figure 31), the observed peak facing displacement for Wall 5 was approximately 60% of that observed for Wall 1 (control structure) and the facing displacement for Wall 6 was only 18% that of the control structure. This is attributed to the relatively greater stiffness of the PET geogrid at higher tensile load levels and longer elapsed time (Figure 7) and the greater stiffness of the wire mesh reinforcement.

2.8 *Reinforcement tensile over-stress*

Figure 34 shows a comparison of predicted reinforcement load in layer 5 of Wall 1 (which was the highest loaded reinforcement layer at the end of the surcharging period) and the predicted value using Coulomb earth pressure theory with $\phi = \delta = 44°$. Superimposed on the figure is the creep-limited strength (3.9 kN/m from Figure 32), which is the tensile load required to achieve the performance limit load for the unmodified PP geogrid in a conventional constant load (creep) test. It should be noted that no reduction in the available strength of the reinforcement has been made to account for installation and/or environmental degradation as would be the case for the design of a field structure. These degradation mechanisms are not significant due to the very careful construction technique used in these experiments and the benign chemical environment. The data shows that for the critical reinforcement layer in the structure, the surcharge load required to achieve the performance limit load of the reinforcement is 42 kPa as determined from Coulomb theory. However, the actual observed surcharge load to achieve the same condition is approximately 92 kPa. Hence, it can be argued that Wall 1 had a surcharge capacity that was approximately 2.2 times the predicted values based on performance limit load as a limit state for Coulomb-based design.

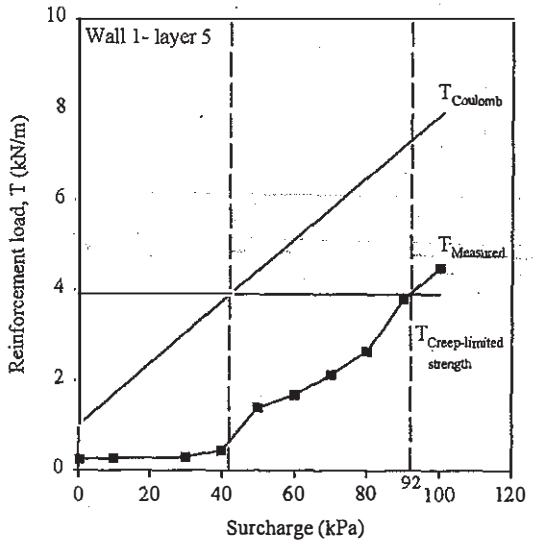

Figure 34. Comparison of predicted and measured reinforcement load for layer 5 of Wall 1.

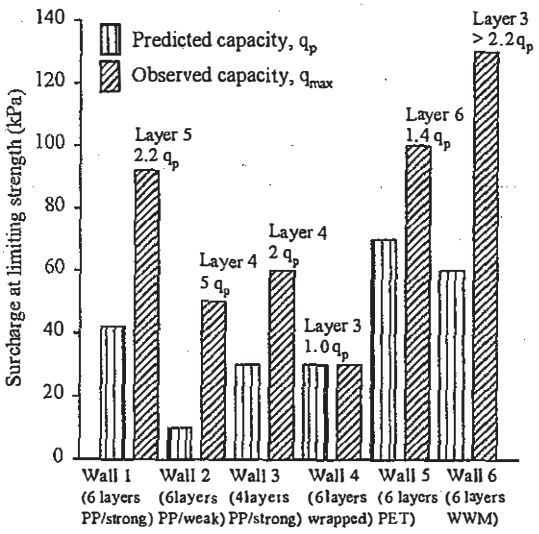

Figure 35. Comparison of predicted and observed surcharge capacity of test walls based on creep-limited strength of the reinforcement.

A similar analysis was carried out for all six wall structures in this investigation. For the PET reinforcement the limit load was taken as 5.1 kN/m (Figure 33) although this value does not imply that tensile loads in excess of this value will lead to excessive straining. This is simply a reference value identifying a relatively minor change in reinforcement stiffness. For the welded wire mesh wall (Wall 6) the yield load of the wire was taken as the limit state for design. The results of all structures are summarised in Figure 35. The data shows that the ratio of observed to predicted surcharge pressure at the limit state for the hard-faced (stiff) walls ranges from 1.4 to 5. Layer 3 in Wall 6 was very close to yield at which time the surcharge capacity of the test facility was reached. In contrast to the hard-faced (stiff) wall, the limit state of reinforcement layer 3 in Wall 4 was achieved at the predicted surcharge level. However, it should be recalled that Wall 4 is an unusually flexible wrapped-face structure. Wrapped-face wall structures in practice are constructed with facing wraps that extend into the reinforced soil zone and may be expected to have a stiffer facing performance. The soil reinforcement material used in this test wall was also extremely extensible. Hence, the accuracy of the predicted surcharge capacity based on Coulomb-based design should not be expected for actual field wrapped-face structures.

Nevertheless, the data shows that there is excessive conservativeness in the design of walls with significant facing stiffness and comparable height to those investigated here, based on conventional limit-equilibrium methods.

3 NUMERICAL MODELLING

The dynamic finite-difference computer code FLAC (Itasca 1998) was used to simulate the response of Walls 1, 2 and 5 up to the end of construction. These walls are nominally identical with the exception of the properties of the reinforcement materials. The numerical models used material mechanical properties for the backfill soil, reinforcement and modular block interfaces that were obtained from independent laboratory tests.

3.1 *Numerical models and material properties*

Figure 36 shows an example of the numerical model for the SRW structures in this research program. The backfill was modelled as a cohesionless granular soil with Mohr-Coulomb failure criterion and dilation angle. The stress-dependent hyperbolic model proposed by Duncan et al. (1980) was used to represent the soil non-linear load-strain response during construction. The hyperbolic parameters were determined from the results of biaxial (plane-strain) tests on RMCC sand specimens (Lee 2000) and are reported in Table 2. The value of backfill dilation angle (ψ) from direct shear tests was found to vary from 9° to 12° for the range of confining pressures in the test walls. A dilation angle value $\psi = 10°$ was chosen for numerical models. The soil peak plane strain friction angle was determined to vary between 42° and 44° for the same range of confining pressure with the best estimate value taken as $\phi = 44°$.

Fixed boundary conditions in both horizontal and vertical directions were assumed for the numerical grid points at the rigid foundation level and in the horizontal direction only at the backfill far-end boundary. The backfill and facing units of each wall model were elevated in lifts of 0.15 m (i.e. the height of one modular block) and the reinforcement layers were placed in the model as each reinforcement elevation was reached.

The compaction of the backfill during construction was simulated by applying a prescribed lateral stress behind the facing column. The effect of

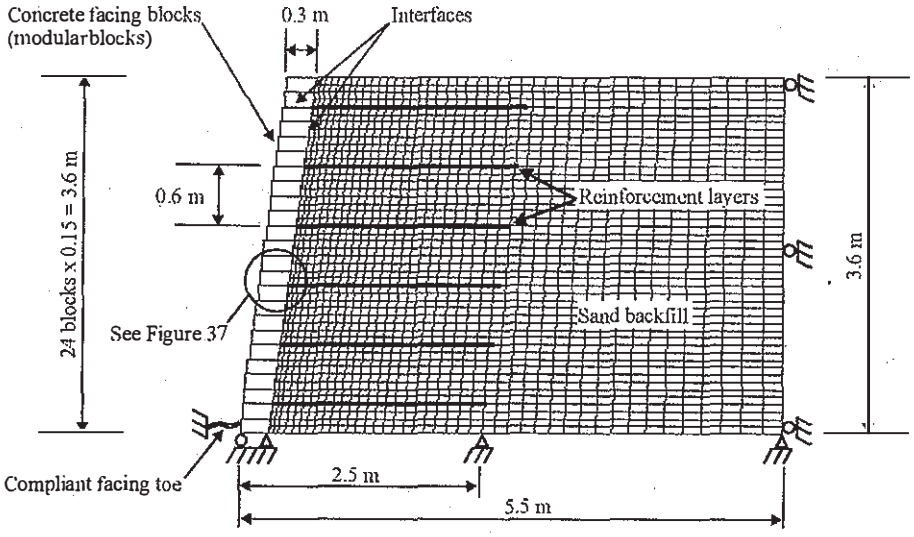

Figure 36. Numerical grid for RMCC segmental retaining walls.

Table 2. Parameter values for the backfill soil model.

Stiffness properties (Hyperbolic model)	Value
K_e (Elastic modulus number)	2000
K_b (Bulk modulus number)	2000
n (Elastic modulus exponent)	0.5
m (Bulk modulus exponent)	0.5
R_f (Failure ratio)	0.73
ν (Poisson's ratio)	0.0 - 0.25
Strength properties	
ϕ (Peak friction angle)	44°
c (Cohesion)	0
ψ (Dilation angle)	10°
ρ (Density - 3% water content)	1700 (kg/m^3)

Note: Soil hyperbolic stiffness parameters are all dimensionless.

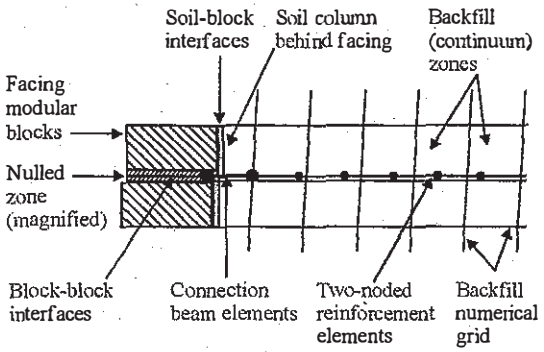

Figure 37. Details of facing-backfill-reinforcement connections.

soil compaction during construction was assumed to be negligible for Walls 1 and 2. However, Wall 5 was constructed with a larger compactor and a greater compaction effort. Therefore, a larger soil compaction stress was introduced in the simulation for Wall 5 and consequently a better match made with observed wall facing displacement measurements. The equivalent compaction effort behind the facing for Walls 1, 2 and 5 was assumed to be 0.25, 0.25 and 1.5 kPa, respectively.

The reinforcement layers were modelled with two-noded elastic-plastic cable elements (Figure 37) with strain-dependent tangential tensile stiffness, $J_t(\varepsilon)$, tensile yield strength, T_y and negligible compressive strength. Figure 38 shows the reinforcement load-strain response represented in the parabolic form:

$$T(\varepsilon) = A\varepsilon - B\varepsilon^2 \qquad (1)$$

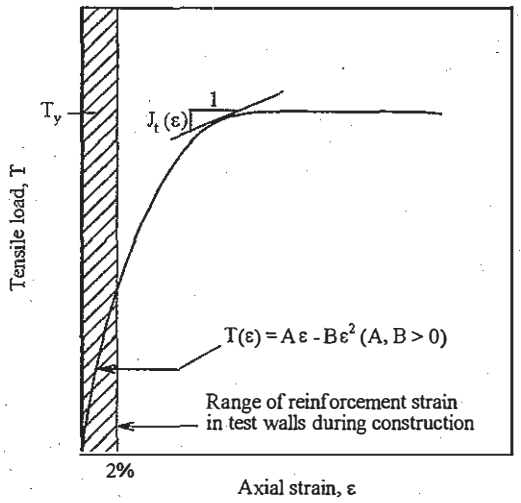

Figure 38. Reinforcement load-strain model implemented in FLAC.

where T is load and ε is strain. The reinforcement strain-dependent tangential tensile stiffness, $J_t(\varepsilon)$, is calculated from Equation 1 as:

$$J_t(\varepsilon) = \frac{dT(\varepsilon)}{d\varepsilon} = A - 2B\varepsilon \quad (2)$$

The parameter A is the initial stiffness modulus and parameter B is the strain-softening coefficient which is a positive value for geosynthetic reinforcement materials with strain-softening characteristic. The construction history of Walls 1, 2 and 5 showed a nearly uniform increase in wall height with time (Figure 13). Therefore, results of in-isolation constant rate of strain (CRS) tests were used to calculate reinforcement stiffness values. The strain-dependent reinforcement stiffness expressions for polypropylene and polyester geogrids were obtained by fitting parabolic curves to the corresponding CRS test results for the range of recorded strains up to the end of construction (i.e. less than 2%).

The interaction between the reinforcement layers and the adjacent zones of the backfill soil continuum was modelled with a grout material. The mechanical characteristics of the grout material, are modelled as a spring-slider system, defined by shear stiffness, k_{bond}, and Mohr-Coulomb type strength parameters defined by cohesion s_{bond} and friction angle δ_{rs}. The stiffness and strength of the reinforcement grout material were set to $k_{bond} = 10^6$ kN/m/m, $s_{bond} = 10^3$ kN/m and $\delta_{rs} = 44°$, respectively. These values resulted in negligible slippage or pullout of reinforcement in the backfill soil and simplified numerical calculations.

The properties of the reinforcement used in numerical simulations of Walls 1, 2 and 5 are presented in Table 3.

The facing modular blocks were modelled as linear elastic continuum zones separated by nulled zones of zero thickness that contain interfaces (Figure 37). The interfaces were modelled as a spring-slider system with given strength and stiffness properties (Itasca 1998). The relative movement of the two interface surfaces is controlled by the interface stiffness in normal (k_n) and tangential (k_s) directions. A recommended rule-of-thumb estimate for maximum interface stiffness values, k_n and k_s is given by (Itasca 1998):

$$k_n = k_s = 10 \times \max\left[\frac{K + \frac{4}{3}G}{(\Delta z)_{min}}\right]_i \quad i = 1, 2, \ldots, n \quad (3)$$

The parameters $(\Delta z)_{min}$, K and G are the smallest dimension in the normal direction, the bulk modulus and shear modulus of the i^{th} continuum zone adjacent to the interface, respectively.

The interface shear strength was modelled with the Mohr-Coulomb failure criterion defined by the interface cohesion and friction angle. Figure 39 shows the interface properties between the facing blocks determined from the results of interface shear tests. Peak interface friction angle and equivalent cohesion values are $\delta_{bb} = 57°$ and $c_{bb} = 45.7$ kPa, respectively. Load-displacement curves for shear tests carried out at vertical load levels representing construction gave interface stiffness values in the range k_{sbb} = 8,000 and 60,000 kN/m/m. A set of parametric studies showed that a value k_{sbb} = 60,000 kN/m/m resulted in facing deformation profiles that gave the best agreement with measured results (Hatami & Bathurst 2001a). The interface friction angle between the backfill and facing blocks was back-calculated from measured toe reactions and the sum of measured connection forces using the facing equilibrium analysis described by Hatami & Bathurst (2001b). The analysis demonstrated that the

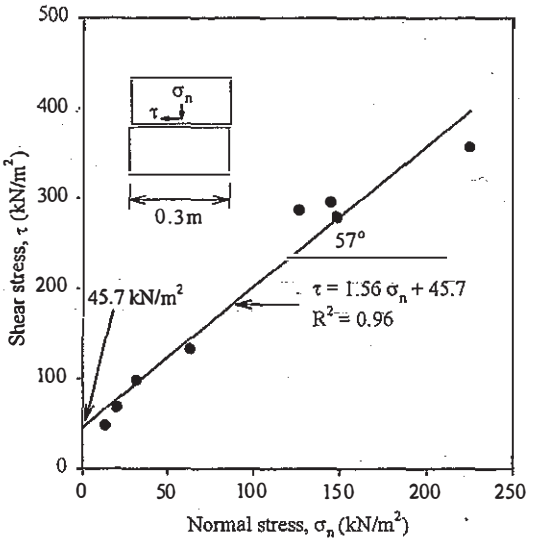

Figure 39. Facing block interface shear strength.

Table 3. Parametric values for the reinforcement models.

Wall	Geogrid material	Reinforcement stiffness $J_t(\varepsilon)$ (kN/m)	Yield strength T_y(kN/m)
1	PP	138 - 1698ε	14
2	PP	69 - 849ε	7
5	PET	185 - 2622ε	16
All walls		δ_{rs} (Reinforcement-soil friction angle)	44°
		k_{bond}	10^6 (kN/m)
		s_{bond}	10^3 (kN/m)

Table 4. Parametric values for the interfaces.

Soil-Block	Value
δ_{sb} (friction angle)	44°
ψ_{sb} (dilation angle)	10°
k_{nsb} (normal stiffness)	0.1×10^6 (kN/m/m)
k_{ssb} (shear stiffness)	10^3 (kN/m/m)
Block-Block	**Value**
δ_{bb} (friction angle)	57°
c_{bb} (cohesion)	45.7 (kPa)
k_{nbb} (normal stiffness)	10^6 (kN/m/m)
k_{sbb} (shear stiffness)	60 (MN/m/m)

actual soil-facing interface friction angle value in the test walls was comparable to the magnitude of the backfill peak friction angle. Table 4 summarises the values for the interface properties used for RMCC segmental walls. The effective (average) horizontal stiffness of the facing toe was determined from the history of measured horizontal toe load and lateral toe displacements.

3.2 *Results*

3.2.1 *Wall facing displacement*

Figure 40 shows the profiles of measured and numerically calculated lateral displacement of individual facing blocks at potentiometer levels (Figure 8) at the end of construction. The measured displacement results are readings from the potentiometers that were positioned against the facing blocks at reinforcement layer levels during construction. Accordingly, the recorded displacement values at each elevation in Figure 40 represent the magnitude of the lateral displacement of the corresponding facing block from the time of installation to the end of construction. The results of facing lateral displacements in Figure 40 show good agreements between recorded and calculated values for the three test walls.

3.2.2 *Toe loads*

Figure 41 shows the history of the measured and calculated horizontal and vertical toe loads for the test walls during construction. The calculated history of toe reactions during construction shows reasonably good agreement with the measured vertical load data. The horizontal loads capture the trend in the data but are less accurate. Nevertheless, the simple interface model for the boundary between the reinforced soil zone and facing column in these tests based on an equivalent fully-mobilised interface friction angle equal to the soil peak plane strain friction angle is a reasonable first approximation.

3.2.3 *Connection loads*

Figure 42 shows the results of measured and calculated reinforcement connection loads in the walls. The data indicates that the magnitude of predicted connection loads are comparable to the measured values but do not capture the trend in the data in each case. This discrepancy highlights the difficulty in modelling local construction-induced variations in the placement of the facing column units and local compaction effects in the vicinity of each connection.

3.2.4 *Reinforcement strains*

Figures 43 and 44 show example measured and calculated strain distribution profiles along the reinforcement layers at the end of construction for two of the wall models. The reinforcement strain experimental data during the construction stage are taken from the strain gauge readings corrected for

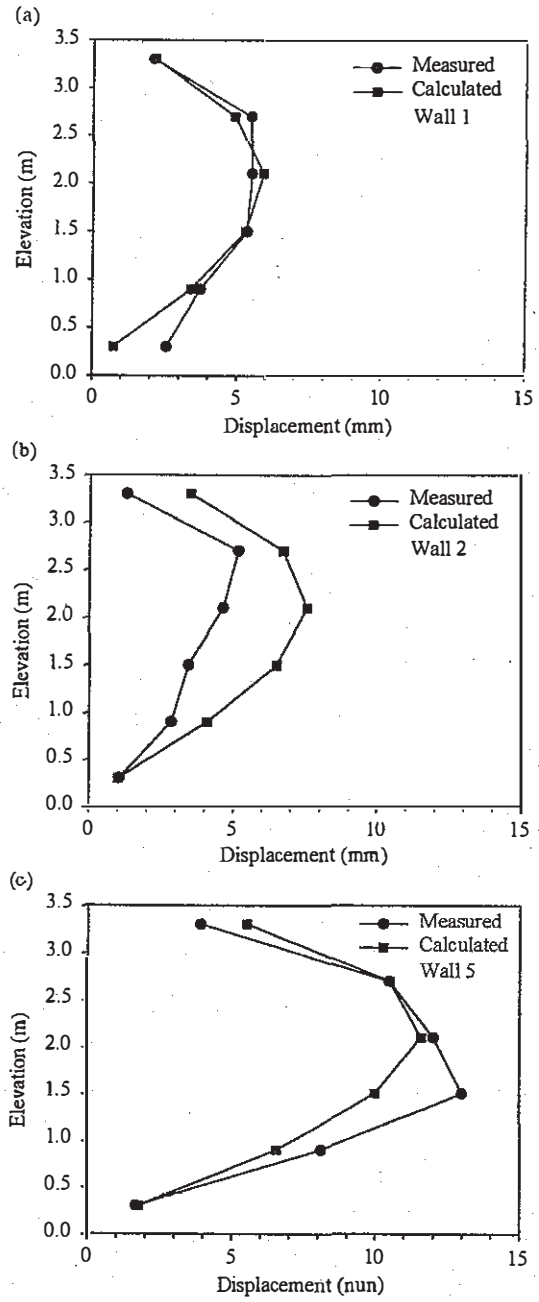

Figure 40. Measured and predicted facing deformations at the end of construction: (a) Wall 1; (b) Wall 2; (c) Wall 5.

under-registration effects. The measured reinforcement strain data for Wall 5 also include the values inferred from the extensometers. The agreement between the calculated and measured reinforcement strain curves is considered to be satisfactory given the generally low strains detected at end of construction and the sensitivity of numerical results to the magnitude of model parameters for reinforcement stiffness behaviour.

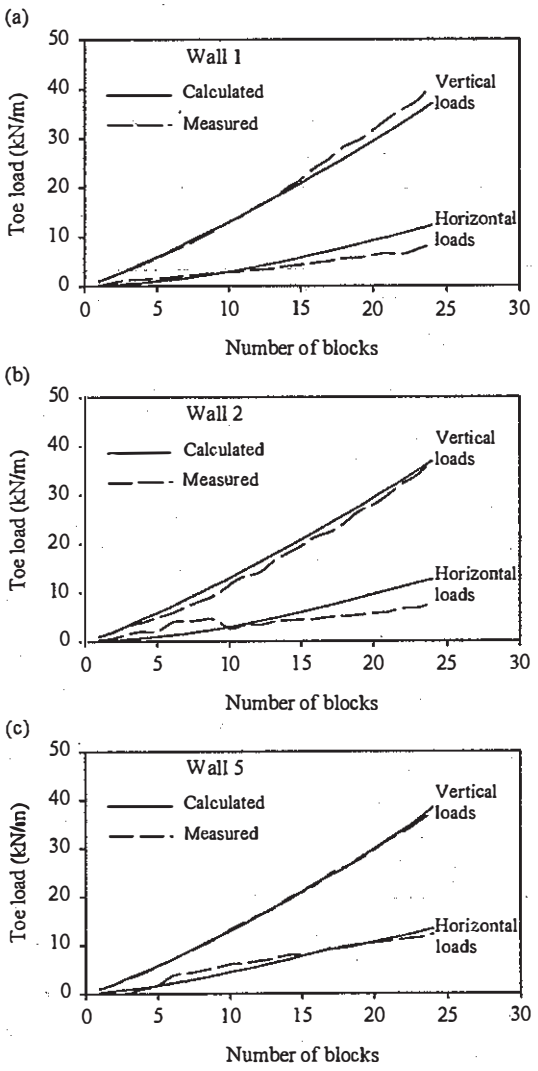

Figure 41. Measured and calculated horizontal and vertical toe loads for the test walls during construction: (a) Wall 1; (b) Wall 2; (c) Wall 5.

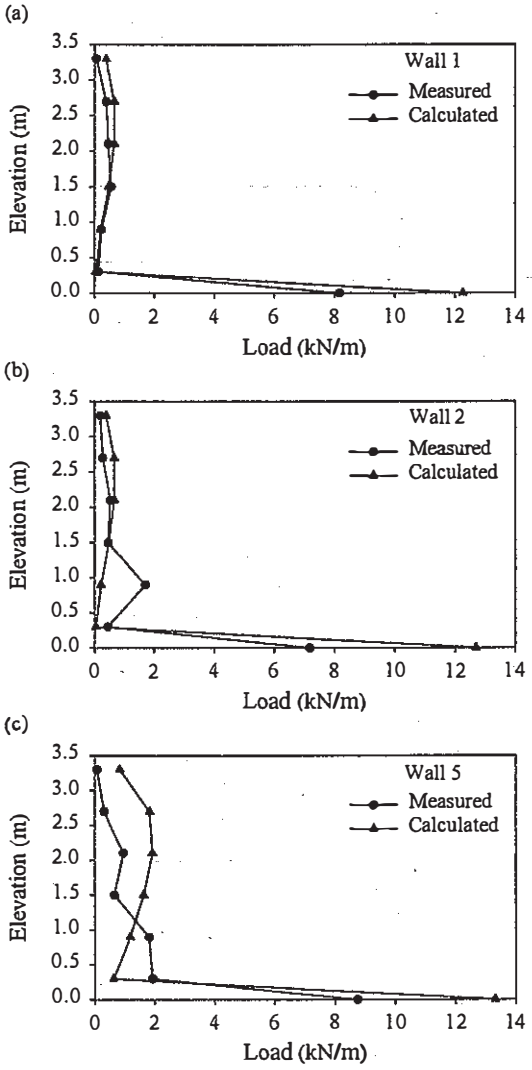

Figure 42. Measured and calculated reinforcement connection and toe loads at the end of construction: (a) Wall 1; (b) Wall 2; (c) Wall 5.

4 CONCLUSIONS

The data collected from the first six walls in this test program is currently under study but some important preliminary observations can be made:

1. Connection loads for the structures with a modular block facing construction were the largest loads in the reinforcement at the end-of-construction condition.
2. The horizontally restrained toe of the wall in these experiments carried a significant portion of the horizontal earth forces acting on the (stiff) hard facing column. This load capacity is not accounted for in current methods of design that use conventional earth pressure theories to predict reinforcement loads and hence is one source of conservatism in current design practice.
3. The selection of the friction angle for the backfill material is another source of conservatism. Peak plane strain friction angles should be selected to reduce the conservatism in the analysis and design of geosynthetic reinforced soil structures constructed with a stiff facing and granular soil.
4. A stiff facing column of the type used in this investigation is a structural element that acts to reduce the magnitude of strains that would otherwise develop in a wall with a perfectly flexible facing.
5. The vertical normal load acting at the toe of the facing column is greater than the sum of the block weights due to soil down-drag forces acting at the back of the facing column. This has important implications to connection design and confirms that for the wall batter used in these experiments the current NCMA method to calculate normal forces at the block interfaces is excessively safe, at least in the short term.
6. Predicted surcharge loads based on Coulomb earth pressure theory were consistently lower than observed values to achieve a target limit-

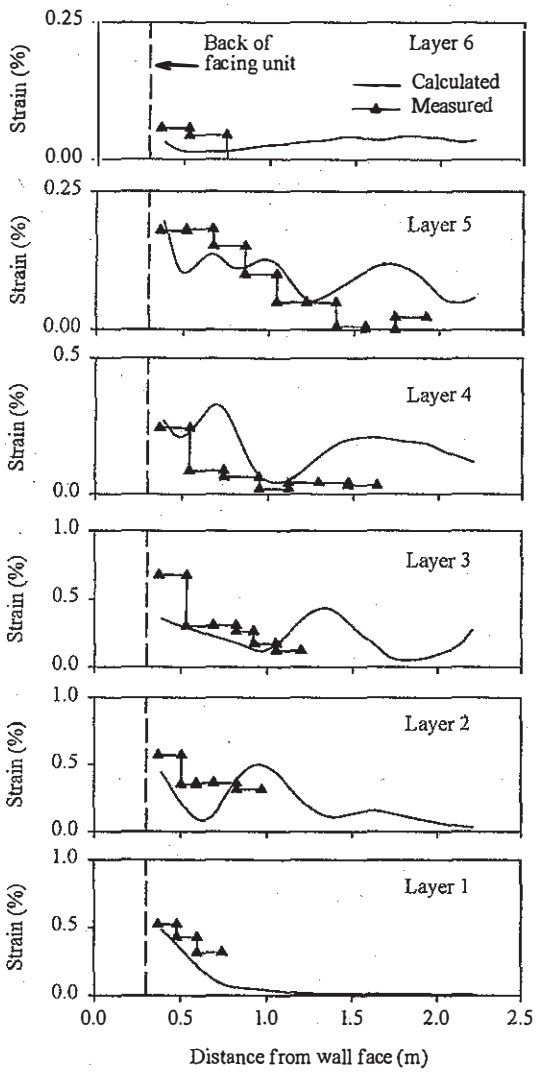

Figure 43. Measured and calculated strain distribution profiles for Wall 1 at the end of construction.

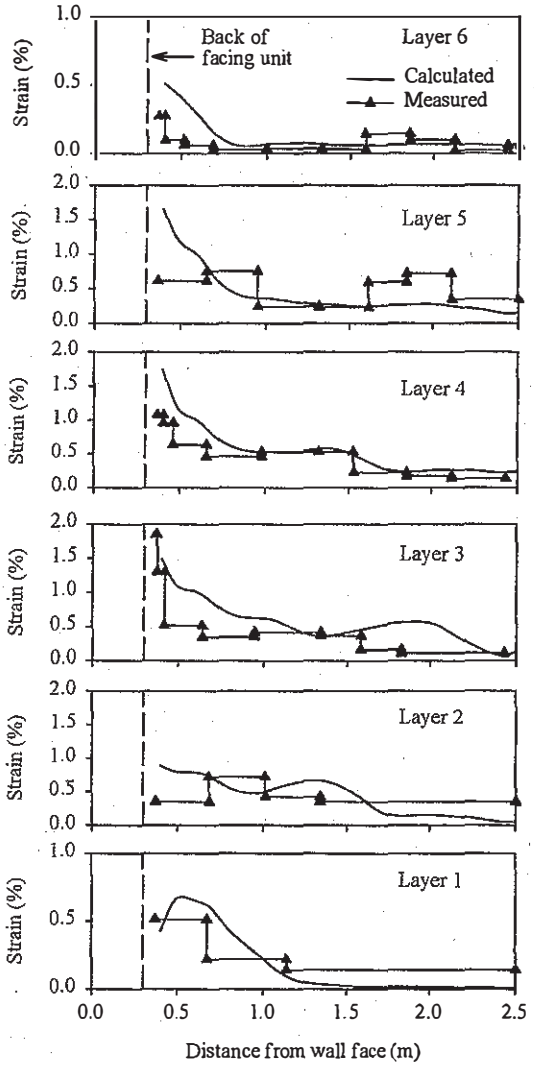

Figure 44. Measured and calculated strain distribution profiles for Wall 5 at the end of construction.

strength value for the hard-faced (stiff) walls in this investigation. The ratio of observed to predicted surcharge pressures ranged from a factor of 1.4 to 5 demonstrating that the general approach for the design of geosynthetic reinforced walls is excessively conservative.

7. For the very flexible wrapped-face wall in this test series, Coulomb earth pressure theory in combination with a contributory area approach and peak plane strain friction angle for the soil, predicted the magnitude of surcharge pressure required to reach the creep-limited strength (limit state) of the critical reinforcement layer in the structure.

The carefully instrumented and monitored walls in this on-going research program have allowed the writers to carry out some preliminary numerical simulations of the hard-faced reinforced soil walls up to the end of construction and to adjust input parameters to match measured results. The simulations were carried out using the commercially available code FLAC. The results of simulation runs gave good agreement for wall deflections and boundary toe forces. The magnitude of predicted connection and reinforcement strains were in reasonable agreement with measured values but the trend in the simulation results was not always captured. The simulation efforts highlight the difficulty to quantify factors such as minor deviations in wall construction technique, soil compaction and the very complex interactions that occur between component materials.

5 FUTURE WORK

Three more reinforced soil walls are planned for this research program. These structures will be designed to isolate the influence of other material properties, geometry and facing type on the response of walls that are variations of Wall 1 (control) described in this paper. For example, walls will be constructed

with different facing batters, smaller reinforcement spacing and lower quality granular fills.

The numerical model described herein will be used to extend the database of test configurations reported here to include higher walls, different soil types, different facing materials and a greater range of reinforcement spacing and properties.

ACKNOWLEDGEMENTS

Funding for the research program described here has been provided by the Washington State Department of Transportation, Alaska Department of Transportation, Arizona Department of Transportation, CALTRANS, Colorado Department of Transportation, Idaho Transportation Department, Minnesota Department of Transportation, New York Department of Transportation, North Dakota Department of Transportation, Oregon Department of Transportation, Utah Department of Transportation, Wyoming Department of Transportation, National Concrete Masonry Association, Reinforced Earth Company, Natural Sciences and Engineering Research Council of Canada, Academic Research Program of the Department of National Defense (Canada) and grants from the Department of Infrastructure and Environment (DND Canada). The authors would like to acknowledge the contribution of graduate students, P. Burgess, N. Vlachopoulos and D. Saunders who carried out the physical experiments described in the paper, numerous research assistants, Risi Stone Systems for provision of the facing units and Terrafix Inc., Strata Systems Inc., and Modular Gabion Systems for provision of the reinforcement materials.

REFERENCES

Allen, T.M. & Bathurst, R.J. 2001. *Prediction of Soil Reinforcement Loads in Mechanically Stabilized Earth (MSE) Walls*, Washington State Department of Transportation, Report WA-RD 522.1, 353 pp.

American Association of State Highway and Transportation Officials (AASHTO) 1996. *Standard specifications for highway bridges.*

American Society for Testing and Materials (ASTM) D4595 1996. *Standard Test Method for Tensile Properties of Geotextiles by the Wide-Width Strip Method.*

Bathurst, R.J. 1990. Instrumentation of geogrid-reinforced roil walls. *Transportation Research Board 1277:* 102-111. Washington, D.C.: National Academy Press.

Bathurst, R.J. 1991. Case study of a monitored propped panel wall. In J. Wu (ed.), *Geosynthetic-reinforced soil retaining walls - Proc. of the Int. Symp. Geosynthetic-Reinforced Soil Retaining Walls, Denver, 8-9 August 1991*: 159-166. Rotterdam: Balkema.

Bathurst, R.J. 1993. Investigation of footing restraint on stability of large-scale reinforced soil wall tests. *Proceedings 46th Canadian Geotech. Conf., Regina, September 1993*: 389-398. British Columbia: Bitech.

Bathurst, R.J. 2000. Lessons learned from full scale model tests of reinforced walls and slopes (Invited keynote paper). *Proc 2nd Asian Geosynthetics Conf., Kuala Lumpur, 29-31 May 2000*: (I) 1-22. Kuala Lumpur: SEAC-IGS.

Bathurst, R.J. & T.M. Allen 2001. Short-tenn strain and deformation behaviour of geosynthetic walls at working stress conditions. Submitted to *Geosynthetics International.*

Bathurst, R.J. & D.J. Benjamin 1990. Failure of a geogrid-reinforced soil wall. *Transportation Research Board 1288:* 109-116. Washington, D.C.: National Academy Press.

Bathurst, R.J. & M.R. Simac 1994. Geosynthetic reinforced segmental retaining wall structures in North America (Invited keynote paper). *5th Int. Conf. Geotextiles, Geomembranes and Related Products, Singapore, 6-9 September 1994*: (4) 1275-1298. Singapore: SEAC-IGS.

Bathurst, R.J., P.M. Jarrett, & S.R. Lescoutre 1988. An instrumented wrap-around geogrid wall. *Proceedings 3rd Canadian Symp. Geosynthetics, Kitchener, Ontario, October 1988*: 71-78. Ontario: Canadian Geotechnical Society.

Bathurst, R.J., M.R. Simac, & R.R. Berg 1993. Review of the NCMA segmental retaining wall design manual for geosynthetic-reinforced structures. *Transportation Research Record 1414*: 16-25. Washington, D.C.: National Academy Press.

Bathurst, R.J., D. Walters, N. Vlachopoulos, P. Burgess, & T.M. Allen 2000. Full scale testing of geosynthetic reinforced walls (Invited keynote paper). In J.G. Zornberg & B.R. Christopher (ed.), *Geotechnical special publication No. 103, Advances in transportation and geoenvironmental systems using geosynthetics, Proc. of sessions of Geo-Denver 2000, Denver, 5-8 August 2000*: 201-217. Denver: ASCE.

Duncan, J.M., P. Byrne, K.S. Wong, & P. Mabry 1980. Strength, stress-strain and bulk modulus parameters for finite-element analysis of stresses and movements in soil masses. *Report No. UCB/GT/80-01*. University of California, Berkeley: Department of Civil Engineering.

Greenwood, J.H., G.T. Kempton, G.R.A. Watts, & D.I. Bush 2000. Twelve year creep tests on geosynthetic reinforcements. *Proceedings of EuroGeo 2, Bologna, 15-18 October 2000*: 333-336. Italy: AGI-IGS.

Geosynthetic Research Institute (GRI) GG1 1992. *Standard test methods for geogrid rib tensile strength.* Drexel University, Philadelphia: Geosynthetic Research Institute.

Hatami, K. & R.J. Bathurst 2001a. Numerical modelling of reinforced soil segmental retaining walls during construction. *Numerical Simulation Study Report submitted to the WSDOT and US-MSE Pooled Fund, October 2001.* Kingston, Ontario: RMCC.

Hatami, K. & R.J. Bathurst 2001b. Modelling static response of a segmental geosynthetic reinforced soil retaining wall using FLAC. *Proceedings 2nd Int. FLAC Symp. Numerical Modeling in Geomechanics, Lyon, October 2001* (in press).

Itasca Consulting Group 1998. FLAC - fast lagrangian analysis of continua (3.40). Minneapolis: Itasca Consulting Group Inc.

Karpurapu, R.G. and R.J. Bathurst 1995. Behaviour of geosynthetic reinforced soil retaining walls using the finite element method, *Computers and Geotechnics*, 17(3): 279-299. Oxford: Elsevier.

Lee, W.F. 2000. Internal stability analyses of geosynthetic reinforced retaining walls. *Ph.D. Thesis.* University of Washington: Department of Civil & Environmental Engineering.

McGown, A., K. Andrawes, K. Yeo, & D. Dubois 1984. The load-strain-time behaviour of tensar geogrids. *Polymer grid reinforcement:* 11-17. London: Thomas Telford.

National Concrete Masonry Association (NCMA) 1997. *Design manual for segmental retaining walls, 2nd edition, second printing.*

Walters, D.L., T.M. Allen, & R.J. Bathurst 2001. Conversion of geosynthetic wall strains to load using in-soil reinforcement modulus. Submitted to *Geosynthetics International.*